# Multi-scale modelling strategy for textile composites based on stochastic reinforcement geometry

Andy Vanaerschot[a,*], Brian N. Cox[b], Stepan V. Lomov[c], Dirk Vandepitte[a]

[a]*KU Leuven, Dept. of Mechanical Engineering, Leuven, Belgium*
[b]*Arachne Consulting, Sherman Oaks, CA, USA*
[c]*KU Leuven, Dept. of Materials Engineering, Leuven, Belgium*

**Abstract**

The quality of high-performance composite structures is difficult to predict or remains unknown. Variability in the macroscopic performance is dominated by the spatial randomness in the geometrical characteristics at the lower scale, especially for textile composites. By identifying the irregularity in the tow reinforcement, an improved assessment of the composites' quality can be obtained. A roadmap consisting of three steps is provided for generating realistic virtual textile specimens spanning multiple unit cells. First, the geometrical variability in the reinforcement structure is experimentally quantified on the meso- and macro-scale in terms of average trend, standard deviation and correlation length. Next, each reinforcement parameter is modelled as an average trend, determined from experiments, added with zero-mean deviations. Depending on the deduced correlation information for each tow path parameter, these fluctuations are generated by advanced simulation techniques such as a Monte Carlo Markov Chain method, a cross-correlated Karhunen-Loève Series Expansion technique or a Fourier Transform method in combination with a Markov Chain algorithm. In a last step, a virtual model of the textile geometry is represented in geometrical modelling software, such at the commercially available WiseTex software.

The multi-scale framework is demonstrated on a carbon-epoxy 2/2 twill woven composite produced by resin transfer moulding. Simulated tow deviations trends replicate the

*Corresponding author. Department of Mechanical Engineering, KU Leuven, Celestijnenlaan 300, 3001 Heverlee, Belgium. Tel.:+32 16322514 ; fax:+32 16322838

*Email address:* Andy.Vanaerschot@kuleuven.be (Andy Vanaerschot)

experimental observations and achieve the target statistics on average.
*Keywords:* Textile composites, Multi-scale modelling, Non-determinism, Probabilistic methods

## 1. Introduction

Composite materials have excellent mechanical properties. Especially the combination of a high strength and stiffness with a low weight offers advantages in energy efficiency for air, ground and water transport. However, the introduction of composites proceeds with difficulty, particularly for safety critical components. One reason is the cost, while another major obstacle remains the uncertain reliability and quality of composite structures. Sufficient instruments are available for the characterisation of the mechanical properties by experiments and numerical simulation. Yet, there is a lack of understanding of how and why the mechanical properties vary across the composite product. Due to the specific nature of each composite with its specific manufacturing process, scatter can be very pronounced which impedes a correct estimate of the quality of the composite component. This variability in the macroscopic performance is directly linked with scatter in the internal structure and constituents at the lower scales.

Variability in the reinforcement structure is frequently omitted or only partially introduced in simulations [1, 2, 3]. For the specific case of textile composites, the reinforcement is adequately modelled by exploiting the hierarchical principle. Predictive models are constructed following a sequence from fibre, tow, textile, preform, to the final composite [4]. To represent its internal geometry, a periodic unit cell model is considered where tow path characteristics are computed based on deterministic inputs such as fibre mechanics, topology, tow dimensions (shape, width, height) and tow spacing. These unit cell descriptions are considered to be repetitive along the entire structure without any variation in the tow position, shape and dimension. However, physical samples do show randomness in the geometrical parameters within a single unit cell and between neighbouring unit cells; tow path descriptors are spatially distributed across the composite [5]. Realistic modelling of internal

geometry should permit the introduction of local variations along each individual tow path. Depending on the response of interest, the variability that is modeled might include all different scales, including the ”fibre scale”, where fibres in the interior of tows are represented as discrete randomly positioned entities, the ”tow scale”, where tows are represented as homogenized entities (fibres smeared into a continuum) with random shape and orientation, the ”unit-cell scale”, representing the minimum group of tow segments needed to establish the repeating unit of a textile architecture, and the ”sub-component scale”, typifying a major structural element and typically comprising $10^2$ $10^3$ unit cells.

Among the different strategies for simulating the randomness in composites using appropriate scaling techniques [6, 7, 8, 9], those that are most likely to lead to accurate predictions of the statistical distributions of composite properties are calibrated by experimental quantification of the material variability. Charmpis et al. [3] present an excellent discussion of how stochastic finite element simulations (SFEM) [10, 11] might be improved if experimental data were to be used to define the random fields that are incorporated within element properties. The desired modelling procedure for textile composites consists of three main steps: (i) collection of material data to define the stochastic geometry of tows (the step of uncertainty quantification and characterisation), (ii) generation of virtual specimens that replicate the measured statistics of the stochastic tow geometry and (iii) formulation of a stochastic multi-scale modelling scheme by which macroscopic material properties, and the variability in those properties, are predicted from the stochastic tow properties. When the first step is missing, analysts are forced to make assumptions regarding the input information for the second and third steps, leading to questionable estimates of the limits of material properties. The more detail that is available in the characterisation of the stochastic material microstructure, the higher the possible fidelity of simulations of damage evolution. In particular, not only are the distributions of material characteristics at any point important, but data defining the correlations between material deviations at different points can also be essential to complete prediction of the performance of a component [3, 7, 12].

This article describes a multi-scale framework to generate realistic representations of

the reinforcement geometry, in which the variability of fibre positioning in a textile is characterised on different scales and fused into virtual specimens that span many unit cells (typically $10^3$-$10^5$ unit cells) while retaining details of stochastic variability of tow geometry within a single unit cell. The article starts with a general overview of existing uncertainty modelling techniques applied to composites, before proposing the multi-scale strategy in section 3. Section 4 discusses the experimental frameworks that are defined to characterise the scatter in the internal geometry over two scales: the short-range, i.e. the unit-cell scale, and the long-range, i.e. the sub-component scale, which incorporates large numbers of unit cells. Next, random instances of tow path parameters are produced using advanced simulation techniques presented in section 5. Tow path features which are only correlated along the length of that tow (”auto-correlation”) can be simulated using the relatively simple concept of the Markov Chain [13] or a Series Expansion algorithm [14], while properties that are correlated both along one tow and between different tows (”cross-correlation”) are produced using a cross-correlated Series Expansion technique [14] or a combination of Fourier analysis and the Markov Chain algorithm [15]. In a final step, virtual models of the entire composite geometry are constructed using the WiseTex software [16], which is a geometry processor for textile fabrics (section 6). Each step throughout the developed framework is demonstrated for a 2/2 twill woven carbon fibre reinforced epoxy composite for which experimental data are already reported in prior publications [17, 18].

## 2. Overview of existing simulation techniques for textile composites

Methods of simulating the effects of random microstructure on composite properties can generally be classified into ”non-intrusive” and ”intrusive” approaches, terminology which we borrow from the field of spectral methods for uncertainty quantification, with applications in, e.g., fluid dynamics [19]. In stochastic spectral analysis the unknown expansion coefficients, appearing in the spectral expansion of the desired solution, might be computed by adding variability to the output of a deterministic solver that represents the system being modelled, or the solver itself might be modified to incorporate stochastic character in the

definition of its kernel. The former case is called as a non-intrusive method, the latter an intrusive method.

In the context of simulating the performance of a composite material with stochastic reinforcement geometry, a non-intrusive method uses a deterministic representation of the reinforcement geometry (e.g., perfectly regular plies in a tape laminate or perfectly regular, periodic tows in a textile composite) and adds stochastic character by assigning material properties to individual material elements that are drawn from statistical distributions; whereas an intrusive method uses representations of the reinforcement geometry that are themselves stochastic. Both non-intrusive and intrusive formulations are often analyzed in a Monte Carlo framework [20], in which instantiations of random material properties (non-intrusive method), or of a random reinforcement geometry (intrusive method), are generated by invoking a pseudo-random number generator; many specimens are generated and the scatter in composite properties are computed [21, 22]. Intrusive methods can generally be decomposed into three groups depending on the manner in which correlations between deviations in the reinforcement geometry are treated, as detailed below.

### *2.1. Non-intrusive simulation techniques*

Non-intrusive simulation techniques introduce the effects of variations in the reinforcement geometry without changing the existing, idealized reinforcement model, but changing local material properties instead.

In the approach of a non-intrusive SFEM [10, 11], the distributions of material properties are often determined by fitting predictions to distributions of predicted lifetime and strength, i.e., by curve-fitting the desired outcome. A more realistic approach seeks to determine the distributions of material properties by independent analysis of how local properties will be affected by measured material randomness, including stochastic reinforcement geometry and other defects. Examples of such work include studies of the compressive strength, and fatigue life under compression-compression loading, of non-crimp fabrics that contain random misalignments of the nominally aligned tows (figure 1(a)). Failure in compression in both 3-D woven composites and triaxially braided composites, under loads aligned with

non-crimp warp or weft tows in the former or axial tows in the latter, is mediated by kink band formation. The fatal kink band forms where the misalignment angle, $\varphi$, of the aligned tows is greatest. The largest values of $\varphi$ expected in the gauge volume of a typical specimen can be estimated as the 95th percentile of measured cumulative probability distributions (CPDs) of $\varphi$, which have been determined by analyzing optical images of cross-sections of the composites (e.g., figure 6 of [23] and figures 3 and 4 of [12]). The value of the local compressive stress $\sigma_c$ at which the kink band will form is well approximated by [24]:

$$\sigma_c = \frac{\tau_c}{\varphi} \tag{1}$$

where $\tau_c$ is the critical shear stress at which the matrix within the tow fails, which can be calibrated by independent tests (Appendix A of [25]; [26]). Combined with analysis of the stress distribution in the composite made using non-stochastic idealisations of the reinforcement geometry, the failure law of equation 1, which amounts to a stochastic assignment of local material strength, because the value of $\varphi$ is a random variable, successfully predicts compressive strength (e.g., figure 1(a); see also figure 11 of [12]). Combined with a law for the degradation of $\tau_c$ with elapsed fatigue cycles, the same approach successfully predicts strength-life (S-N) curves for 3-D woven composites under cyclic compressive loading [27]. While these studies used a single measure of the distribution of $\phi$ to predict the most likely compressive strength, a distribution of compressive strengths for an ensemble of specimens could be predicted by the same procedure by using the complete measured distribution of $\varphi$ (see section 2.2.1).

Thus non-intrusive methods can be effective in a top-down engineering strategy for predicting the scatter in many engineering properties, provided relatively rich experimental data are used to calibrate the embedded statistical distributions. However, in the absence of detailed representations of stochastic reinforcement geometry, the potential accuracy of predictions of performance is limited.

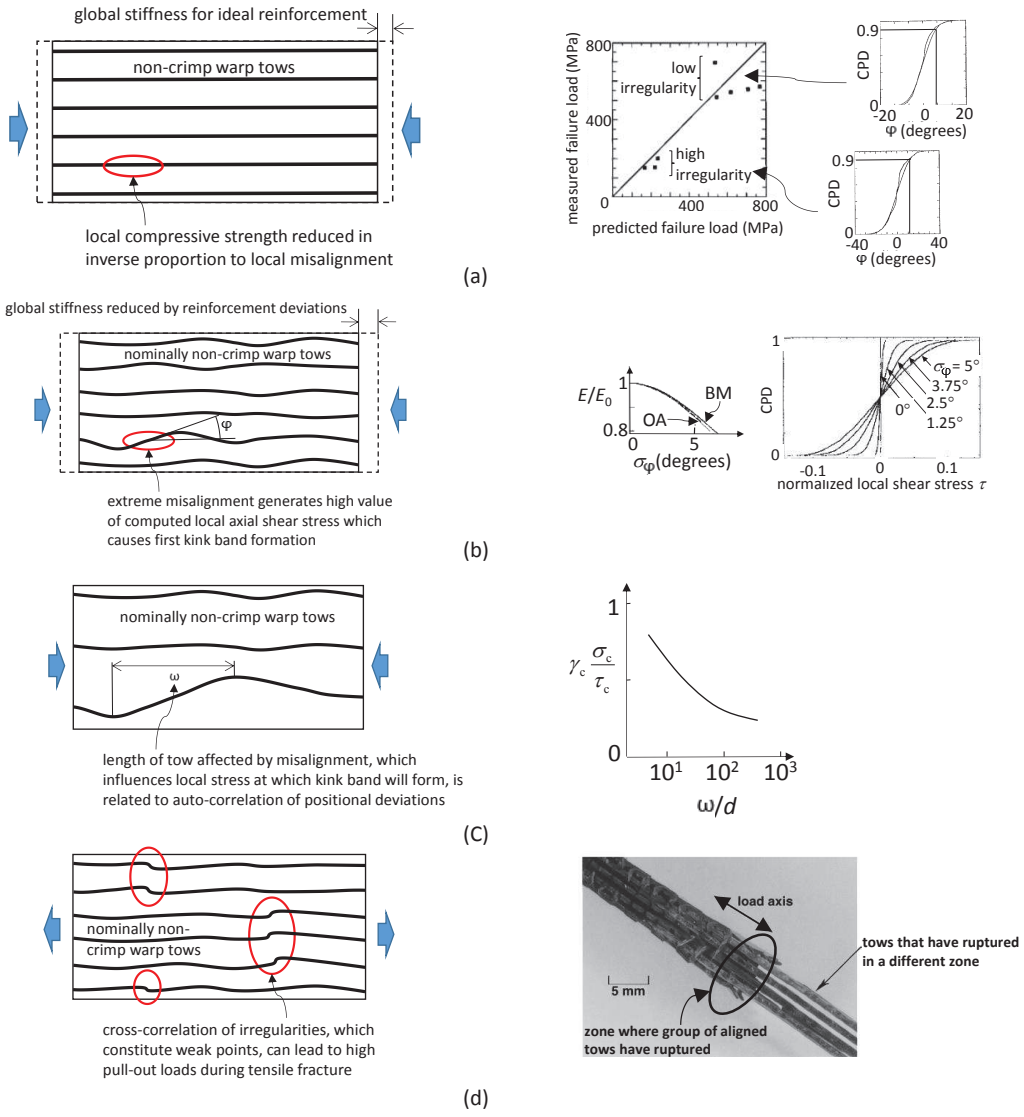


Figure 1: (a) non-intrusive model: stress analysis of composite with ideal reinforcement geometry is combined with the measured CPD for the misalignment angle $\varphi$ (illustrated in (b)) and the measured critical local shear stress $\tau_c$ to correctly predict compressive strength for two groups of 3-D woven composites with differing degrees of irregularity (after [25]). (b) intrusive model with uncorrelated deviations: reinforcement model includes random misalignments of tows. Predictions include the global stiffness reduction $E/E_0$, computed either using analytical orientation averaging formulae "OA" or finite element methods "BM"; and CPDs for the local axial shear stress $\tau$ corresponding to different assumed distributions of $\varphi$, represented by the second moment $\sigma_\varphi$, computed using finite element methods. The shear stress $\tau$ drives kink formation in compression. (c) intrusive model with auto-correlated deviations: correlation length for auto-correlated deviations is related to size of domain of extreme misalignment, which influences local stress at which kink band will form, plotted in normalized form as a function of the ratio $\omega/d$, where $d$ is the fibre diameter (after [28]). (d) intrusive model with cross-correlated deviations: clustering of defects can lead to tow rupture events being concentrated in two or more zones, which enables sustained, high pullout loads and high tensile fracture toughness.

### *2.2. Intrusive simulation techniques*

#### *2.2.1. Methods based on spatially uncorrelated deviations*

The first group of intrusive methods introduces random deviations into the positions or shapes of tows, thus creating a stochastic reinforcement geometry, but treats the deviations at different locations as statistically uncorrelated (figure 1(b))

One example is a study of non-crimp 3-D woven composites, in which the positions of nominally straight warp or weft tows were varied in a stochastic geometrical model of the composite according to statistical distributions determined by analyzing images of specimens, as described above [23, 12]. Predictions were made of the rate at which macroscopic stiffness would decline as the average tow deviation increased; predictions made by finite element (FE) analysis (using the Binary Model formulation, in which tows are represented a 1-D elements embedded in a 3-D effective medium) agree almost exactly with predictions made using orientation averaging [29, 30], an analytical method derived by assuming isostrain conditions (figure 3 of [31]). Furthermore, when the stochastic reinforcement model is calibrated using measured distributions of misalignment, both methods of analysis agree well with experiments [23], implying that spatial correlations of alignment deviations may have little effect on macroscopic elasticity.

FE analyses executed within a Monte Carlo framework also yield predictions of the statistical distribution of the local stresses that arise under far-field loads in the presence of populations of random local tow deviations. With the variance in local stress conditions computed, more accurate predictions can be made of the statistical distribution of the global stress at which kink bands occur than are possible using the non-intrusive method discussed in section 2.1 (e.g., figure 7 of [31]). The extent to which spatial correlations among the deviations in tow alignment might change the predicted distributions of local stress remains to be examined.

Instead of using experimental data, the amplitude of deviations in tow positions, in models in which spatial correlations have been neglected, have also been calibrated by matching predicted macroscopic mechanical behaviour with experimental results [32, 33]; and com-

puted by simulating the effect of disruptive mechanical loads on an initially ideal preform.

### *2.2.2. Methods including correlations between the deviations at pairs of points along a single tow*

In the second group of intrusive methods, spatial correlations are introduced among the deviations from ideal tow geometry that exist at pairs of points, but only for points residing on the same tow. We refer to this class of correlations as ”auto-correlations”. Given this restriction, stochastic geometrical parameters can be considered as *random fields* generated by a stochastic process, terminology that implies the presence of a single continuous independent variable, which, in the present application, is the position along a tow. In statistical physics, the single variable would often be a time variable. If the stochastic process is a stationary process, i.e., is governed by statistics that do not vary along the tow, and is characterised by Gaussian distributions, it is fully defined by the first two moments of the data and their auto-correlations. Three different treatments of such models in the literature can be distinguished:

- In cases where correlation data are lacking, assumptions need to be made on the properties of the stochastic process. Examples of such modelling of tow paths in textiles is found in [34] and [35], where parametric trigonometric functions are used to represent the amplitude, wavelength and/or phase of the tow path parameters that are varied randomly from point to point on a grid with a fixed interval.

- Where experimental correlation information is available, the stochastic fields can be calibrated to reproduce the correlation data. Realisations of such random fields for textile features are obtained by decomposition of the correlation matrix by the Cholesky factorisation [36] or using Principal Component Analysis [37, 38], in combination with a vector of independent standard Gaussian random variables. Of these approaches, the Principal Component Analysis is more efficient for highly correlated vectors [39], and minimizes the dimensionality of representations.

- Auto-correlated deviations can also be produced for tows within textiles without decomposing the correlation matrix by using the Monte Carlo method to instantiate a Markov Chain model [40, 41]. Tow deviations are generated by marching sequentially from grid point to grid point along a tow path, using a probability transition matrix that can be calibrated using experimental data for tow statistics. A post-processing operation is required to remove unphysical spikes in the generated tow path, which arise from the discreteness of the representation.

Simulations of composite performance that might investigate the possible influence of auto-correlations among tow deviations upon macroscopic properties have not yet appeared. Properties that are likely to be influenced include compressive failure due to kink band formation: the critical stress for a kink band event depends on the size of the domain of misaligned fibres in a composite, falling from high values as the domain size increases until it reaches a plateau value above a critical domain size [28]. In a textile composite, the size of a misalignment domain is related to the correlation length for tow alignment deviations along a single tow (figure 1(c)).

#### *2.2.3. Methods including correlations between the deviations at pairs of points on different tows*

In the third group of intrusive methods, spatial correlations are introduced among the deviations from ideal tow geometry that exist at pairs of points on different tows. We refer to this class of correlations as ”cross-correlations”.In the presence of cross-correlations, stochastic processes, whether analyzed by correlation matrices or the Markov Chain methodology, are no longer an adequate representation. Techniques are needed that accurately simulate the correlations in all directions: along the tow and between neighbouring tows.

The simultaneous reproduction of the auto- and cross-correlation structure of a single uncertain parameter demands more advanced generation techniques developed in the field of stochastic mechanics. An overview of extensions to the previous procedures is:

- To acquire realisations of cross-correlated stochastic functions using the Cholesky

decomposition, an anisotropic correlation matrix must be defined that represents the correlation information both along and between the tow directions. This is determined by defining a multi-dimensional normal distribution which can be described by e.g. a two-dimensional (2-D) extension of the Ornstein-Uhlenbeck process, calibrated to mach the required covariance matrix [36].

- A methodology developed by Vořechovský [38] permits realisations of cross-correlated random fields based on the Karhunen-Loève (K-L) Series Expansion. The procedure was originally used to model correlated material properties in concrete, but is generally applicable for modelling of a set of stochastic fields that share an identical auto-correlation function and of which the cross-correlation can be defined by a cross-correlation coefficient. When applied to textile structures, each tow can be represented by a single random field [14].

- Analysis of cross-correlations in textile structures has also been demonstrated by combining discrete Fourier Transform analysis with the Markov Chain algorithm. Tow packing density deviations (deviations that vary relatively rapidly perpendicular to the tow direction) are generated using random values of the amplitude and phase of each Fourier component taken from experimental distributions. Relatively slow variations of the Fourier coefficients along the tow direction are then analyzed using the Markov Chain algorithm for amplitudes and a random-walk algorithm for phases. An inverse Fourier transform provides a virtual specimen generator, recreating corresponding deviation values at all grid points [15, 42].

As will be demonstrated below, cross-correlations among tow deviations over long gauge-lengths (the sub-component scale) imply variations in the tow packing density, which will influence load distribution in a textile component and therefore global stiffness and ultimate load. Over shorter gauge lengths, cross-correlations in tow deviations have been shown to have a potentially strong effect on fracture toughness under tensile loads. Under loads that are aligned with the warp direction, non-crimp 3-D woven composites occasion-

ally exhibit anomalously high toughness, which arises because high loads continue to be sustained even after all the aligned tows in the test specimen have failed [43]. Load transfer is sustained by friction effects during the pull-out of the broken tow ends across the fracture plane. However, simulations show that a pre-requisite for attaining the high measured toughness values is the presence of preferred planes on which individual tows rupture (figure 1(d)) [43]. A reasonable surmise is that the rupture sites are spatially correlated because defects in the tow geometry are correlated (defects in tow geometry tend to weaken the tow). The correlations desired for achieving high fracture toughness are cross-correlations, referring to deviations on neighboring tows.

### *2.3. Relation of geometrical structure to the material properties*

The above examples reinforce the expectation that textile composite properties, and especially the scatter in properties, are related to the distribution of geometrical imperfections in the reinforcing tows. In the following, we review recent advances in quantifying such imperfections on the scale of the tow and the scale of the sub-component. Imperfections on the scale of the individual fibre within a single tow will not be considered here, although recent experimental analyses have appeared elsewhere [44, 45, 46]. The new analyses have benefited greatly from the advent of rapid 3-D imaging techniques, especially those based on high-resolution computed tomography but also those based on automated sectioning, and advanced 2-D digital correlation image analysis, which yields data over large fields of view. The description of stochastic variability in tow geometry is far more complete than was possible in the era in which the examples of figure 1 were generated and will justify much more ambitious empirically-grounded analyses of composite performance.

## 3. Multi-scale strategy for representing reinforcement variability

We address the measurement and theoretical description of variability in the geometry of textile reinforcement over different scales, culminating in algorithms that generate virtual woven specimens that replicate the statistics of experimental samples. We do not pursue the question of how such virtual specimens can be used in high-fidelity simulations to explore

the role of material randomness in damage evolution, but refer the reader to a survey of recent work on this topic in which the damage is represented as multiple discrete cracks [42]. We further restrict consideration to nominally periodic textiles. The question of how the techniques developed for periodic cases might be adapted to quantify randomness in non-periodic textile preforms, such as developed for integrally-woven structures [47, 48] with symmetry-breaking features (sandwiches, heat exchangers, airfoils, etc.) is left for future work. The presence of nominal periodicity simplifies analysis and greatly increases the information content of a given specimen.

In this work, randomness in the numerical models is considered at the meso-scale (or the unit-cell scale) and macro-level (or the sub-component scale); scatter in the matrix and fibre properties is not considered here, but we note that fibre strength may be correlated with geometrical imperfections, because the latter indicate that the reinforcement has suffered some local deformation. The variability of each tow path is defined for the centroid coordinates $(x, y, z)$, tow aspect ratio $AR$, tow area $A$ and tow orientation $\theta$ of a tow's cross-section which experience shows offer a reasonably complete description of woven tows in a number of cases that have been studied. Figure 2 presents an overview of the multi-scale framework, where three main steps can be distinguished in obtaining random representations:

1. **Collection and statistical analysis of experimental data**
   (a) Characterisation of the short-range variability (meso-scale) using samples close in size to the unit cell.
   (b) Characterisation of the long-range variability (macro-scale) using samples spanning many unit cells.
   (c) Statistical analysis of the tow path and shape parameters in terms of average trends, standard deviation and correlation lengths.
2. **Generating instantiations of stochastic textile reinforcement using multi-scale modelling**
   (a) Replication of average trends in the experimental data.
   (b) Generation of zero-mean deviations that match measured short- and long-range

correlations along each tow path.

(c) Generation of zero-mean deviations that match measured short- and long-range correlations between pairs of tows.

3. **Construction of virtual specimens in a geometrical modelling software**

(a) Generation of non-stochastic geometrical model of the tow architecture using topological ordering rules and tow characteristics supplied by the preform manufacturer.

(b) Superposition of stochastic tow path and shape deviations on the non-stochastic geometric model.

(c) Meshing of the geometrical model for use in FE calculations and attribution of material properties to each computational element that are derived from fibre and matrix properties supplied by the manufacturer.

In this paper, we detail the execution of these three steps, but we stop short of presenting simulations of textile composite performance; simulations of damage evolution, along with the definition of the experimental and analytical techniques that can be used to calibrate failure criteria and fracture laws, can be found elsewhere [42]. All statistical analysis described below has been implemented in the Matlab application. The non-stochastic geometrical model of the preform (Step 3a) was generated using the commercially available WiseTex software package [16]. The examples describe a 2/2 twill weave of orthogonal warp and weft tows, which is a two-dimensional textile in the sense that it comprises a single relatively thin layer. When other topologies are considered, additional parameters enter the statistical analysis, e.g. the braid angle for braids and the distortion of the Z-yarn in case of three-dimensional non-crimp fabrics (e.g., angle interlock or orthogonal interlock).

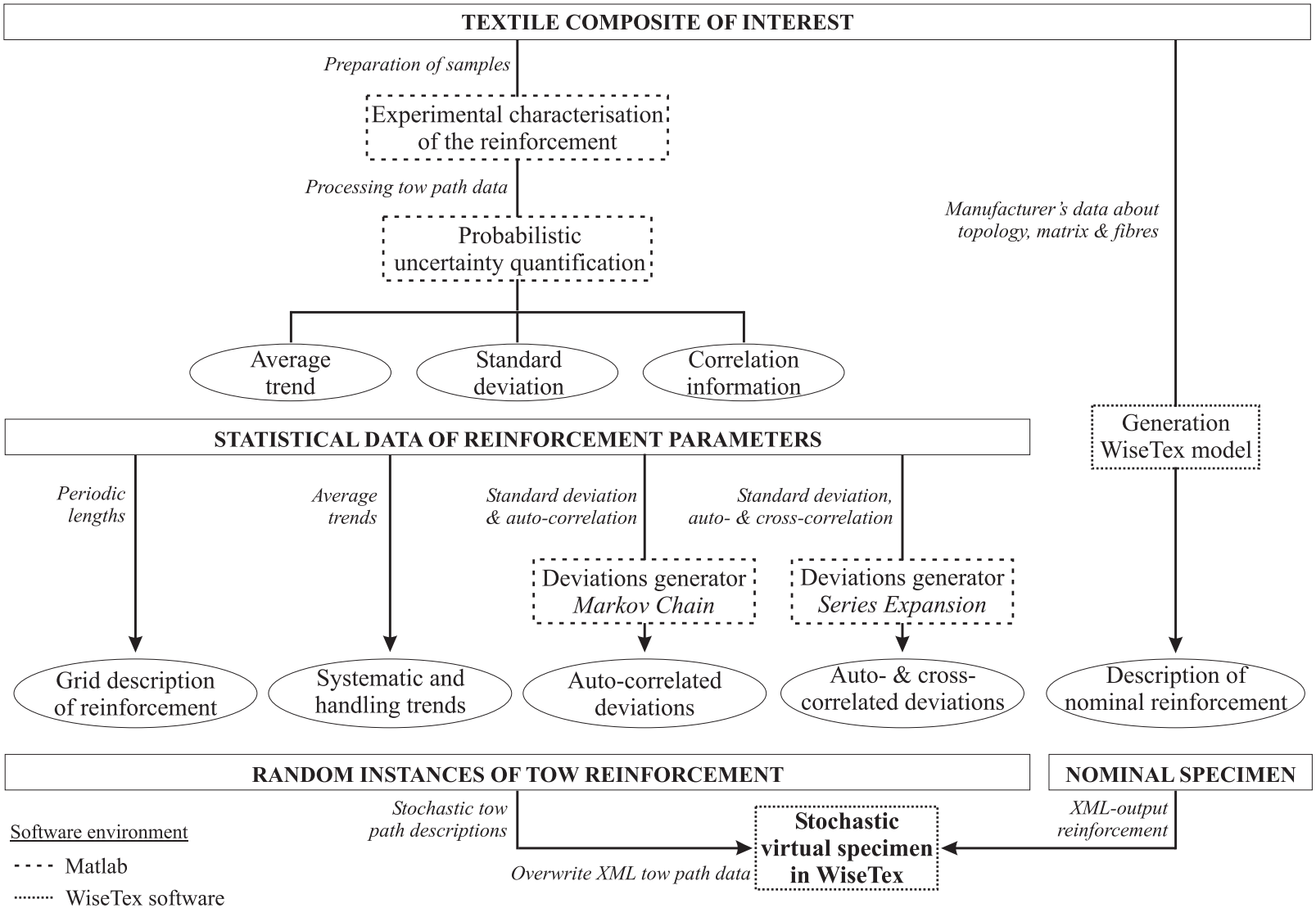


Figure 2: Multi-scale framework.

## 4. Collection and statistical analysis of experimental data (step 1)

### *4.1. Experimental framework*

#### *4.1.1. Experimental quantification of variation in geometry*

Analysis of the experimental data yields statistical metrics, which become the targets for reconstruction algorithms that generate stochastic virtual specimens: a large ensemble of instantiations of virtual specimens must have statistics that match the experimentally determined targets.

Geometrical variability arises within a single unit cell (short-range or meso-scale) and over many unit cells (long-range or macro-scale). Over the short range, 3-D geometrical information, including tow position and shape sampled over a grid that is dense compared to the unit cell, can be collected using micron-resolution X-ray computed tomography (micro-CT). Over the long range, where much larger samples must be dealt with, geometrical information is commonly restricted to positional measurements, sampled over a relatively coarse grid, with spacing comparable to the tow width or to the unit cell size. Long-range positional measurements can be acquired for all tows using relatively low-resolution X-ray CT, or, for those tows that appear on the surface of the specimen, using optical imaging.

Information about a tow's position is stored as the locus of its centroid, which is defined as a 2-D vector of positional coordinates perpendicular to the nominal tow direction: one component lies in the through-thickness direction, $z$, and the other in the orthogonal in-plane direction, $\rho$. The tows are assumed inextensible, an excellent approximation for the magnitudes of loads that arise before a composite is consolidated, and therefore positional deviations along the tow's axis are not independent variables and need not be quantified (they are implied by the lateral deviations). A minimal set of information about a tow's shape comprises the aspect ratio $AR$, the area $A$, and the orientation $\theta$ of the axis along which the shape has its maximum moment, measured on a sequence of cross-sections [49, 40, 17, 13]. Information obtained by micro-CT at the unit-cell scale is relatively complete: for each tow in a sample, the tow path centroids ($(\rho, z)$) and shape parameters $AR$, $A$, and $\theta$ are available. Long-range data are restricted to positional information, although low-

resolution CT may yield approximate data for tow shapes. If long-range data are acquired by analysing single optical images, they are restricted to the in-plane centroid coordinate, $\rho$ [18], but, if they are acquired using 3-D digital image correlation (DIC), they can include both $\rho$ and the out-of-plane deflection $z$ [15].

Data for textiles can be separated according to the type or "genus" of the tow to which they refer, where tows of the same genus are nominally equivalent according to the definition of the textile architecture. For example, in the 2/2 twill weave analysed in section 4.2 and presented in figure 3, warp tows all belong to one genus, while weft tows belong to a second. In a 3-D weave, several distinct genuses of either warp or weft tows may exist [49, 40, 50].

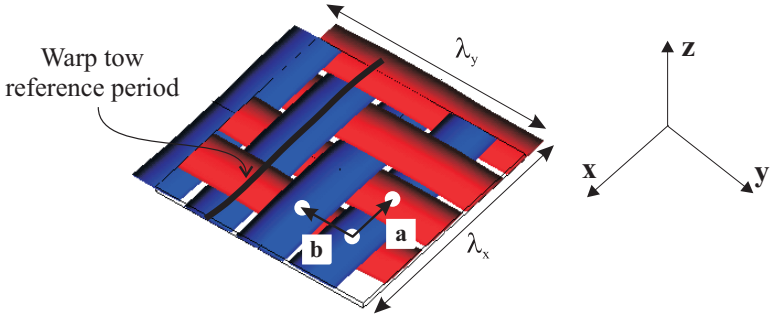


Figure 3: Illustrative WiseTex model of the weave architecture, built as elliptical cross-sections following undulating pathways that match the 2/2 twill cross-over pattern, but not yet informed by experimentally determined geometrical characteristics. The x-axis and y-axis of the coordinate system are respectively parallel to the warp and weft direction. The marked lattice vectors **a** and **b** are used for collating data from tows of the same genus. For example, warp tow collation for long-range data is done by shifting warp tow $j$, with $j = 2, .., N_{warp}$ and $N_{warp}$ the number of warp tows in the specimen, through the vector $modulo[j, 4]\mathbf{a} + (j-1)\mathbf{b}$, so that it lies over warp tow $j = 1$.

For woven textiles, we define a global coordinate system in which warp tows lie nominally in the $x$-direction, weft tows lie nominally in the $y$-direction, and the $z$-direction is the through-thickness direction (figures 3 and 4). The directions of the coordinate axes are determined by finding the best fit of parallel straight lines to the data for all warp tows and all weft tows, subject to the restrictions that the set of lines fitting warp and weft tows must be orthogonal and the spacing for warp or weft tows of any genus must equal $\lambda_x/N_g$ or $\lambda_y/N_g$, respectively, where $\lambda_x$ and $\lambda_y$ are dimensions of the unit cell in warp and weft direction, respectively, and $N_g$ the number of tows of a particular genus per unit cell. This operation

results in a hypothetical perfect lattice of straight, regularly spaced tows, which is an evident choice for textiles consisting of continuous tows. Next, the actual position of any tow in a real or virtual specimen is defined relative to the corresponding straight line in the regular lattice. The lattice is discretised with uniform spacing which differs for either short-range or long-range data (figure 4). To analyse both the short- and long-range data, a system of four discrete rectangular 2-D lattices is generated, comprising one pair of relatively sparse grids for generating long-range positional variations for warp and weft tows (figure 5, and one pair of relatively dense grids for generating short-range positional variations for warp and weft tows (figure 4). The spacing of rows is set to the experimentally determined spacing for either warp or weft tows. The grid spacing along rows is either commensurate with the unit cell size (grids for long-range variations) or much smaller than the unit cell size (grids for short-range variations). It is convenient, although not necessary, to define grid locations so that the grid for long-range variations coincides with a subset of the grid for short-range variations.

For the 2/2 twill weave in figure 3, four tows of each genus occupy each unit cell ($N_g = 4$ for both warp and weft tows) and the spacing of the tows of the same genus is uniform within the unit cell. For 3-D weaves where more than one genus of warp or weft tows is present, the offset of one genus from the other is allowed to vary in the fitting procedure and tows of different genus may not be uniformly spaced within the unit cell [50]. However they are each separately uniform in their spacing over many unit cells.

*4.1.2. Statistical analysis at the unit cell scale*

In analyzing short-range experimental data (the unit-cell scale), advantage is taken of the expected periodicity of the textile. Each tow parameter characterizing position or shape for each tow genus can be decomposed into systematic, non-stochastic variations, which describe the average positional and shape variations imposed on a tow by the interlacing pattern of the weave over the domain of the unit cell, and stochastic deviations, which describe random departures from this average behavior. For parameter $\varepsilon \in \{\rho, z, AR, A, \theta\}$,

with $\rho = y$ or $x$ for warp and weft tows, respectively, we write

$$\varepsilon_i^{(j,t,s)} = < \varepsilon_i^{(j,t,s)} > + \epsilon_i^{(j,t,s)} \tag{2}$$

where $\epsilon_i^{(j,t,s)}$ is the zero-mean deviation from the systematic value $< \varepsilon_i^{(j,t,s)} >$ at location $i$ ($i = 1..N_i$) along the tow $j$ ($j = 1..N_g$) of tow genus $t$ in ply $s$. The label $s$ refers to the ply number, for cases where a laminate of stacked plies is considered.

The systematic trends are identified using the method of "reference period collation" (figure 4) [49, 40]. For each tow genus, a reference period, whose length equals one dimension of the unit cell ($\lambda_x$ or $\lambda_y$), is defined such that any point on any tow of that genus can be mapped onto the reference period by translation through a vector $k/N_{j,y}\mathbf{a} + l/N_{j,x}\mathbf{b}$, where $||\mathbf{a}|| = \lambda_x$ and $||\mathbf{b}|| = \lambda_y$ are lattice vectors, $N_{j,x}$ and $N_{j,y}$ chosen equal to the total number of warp and weft tows, respectively, per unit cell, and $k$ and $l$ are integers [49]. For 3-D weaves, collation could involve more complicated translation vectors in general, but would be entirely analogous. An example can be found in [50]. Figures 4(b) and 4(c) present this collation of all data for the tow genus onto a single reference period to determine the mean trend. Deviations in the short-range data are then defined by comparing the data for any tow at any location with the systematic trend curve at that position, which is created by translating the trend defined on the reference period through the appropriate lattice vector (figures 4(d)). While figure 4 exemplifies reference period collation for one positional coordinate, an exactly similar procedure can be defined for any tow characteristic.

*4.1.3. Statistical analysis at the sub-component scale*

The few high-quality long-range data sets that have been published to date for woven textiles share the characteristic that the largest amplitude deviations in the positions of tows have wavelengths that are comparable to, or slightly greater than, the specimen size. Since the amplitude tends to be much larger than that of deviations with shorter wavelengths, down to the unit cell size, we conjecture that they may have a different source. Since, furthermore, the wavelength is consistent with that expected if the specimen were to be gripped near its

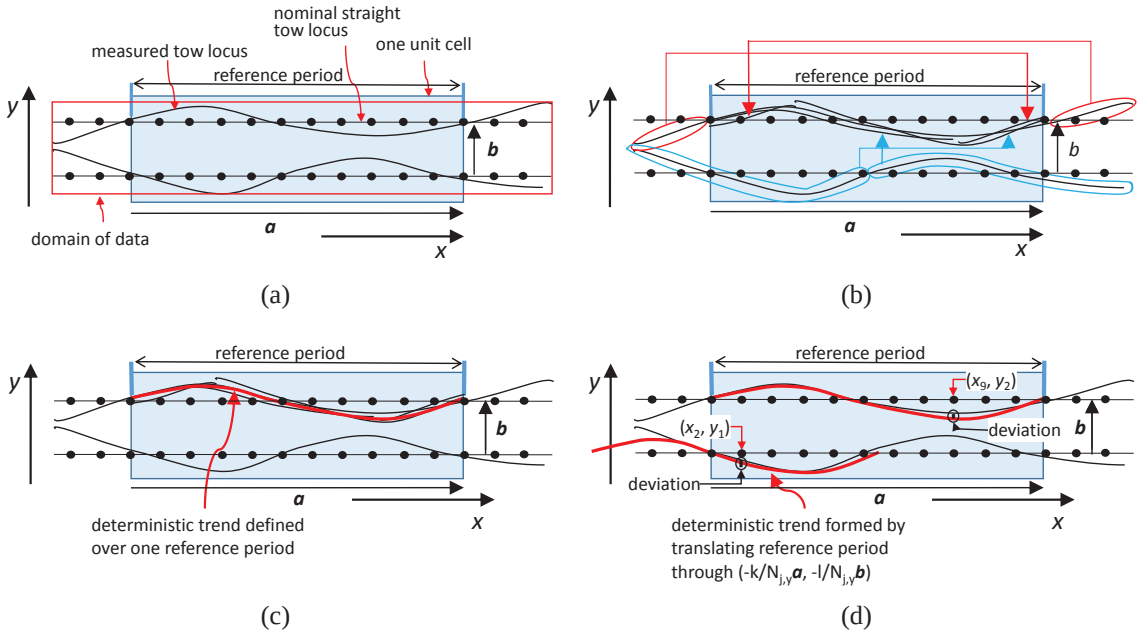


Figure 4: Reference period collation for short-range data, exemplified for the out-of-plane positional coordinate of tows. (a) Data collected for a specimen whose size is slightly larger than the unit cell, which contains two warp tows with staggered phases in the weave. (b) Collation of data onto a single ”reference period”, by shifting data for segments of tows through lattice vectors $(k/N_{j,y}\mathbf{a}, l/N_{j,x}\mathbf{b})$. (c) Averaging of the collated data defines the systematic trend for the positional parameter (red curve). (d) When the systematic trend curve defined on the reference period is translated by a lattice vector $(k/N_{j,y}\mathbf{a}, l/N_{j,x}\mathbf{b})$, the deviation of the positional parameter from the systematic trend can be found for any grid point, as illustrated for two grid points.

periphery and subjected to distorting loads, we conjecture that the largest wavelength deviations were created by handling of the fabric after it had left the loom, whereas deviations characterized by shorter wavelengths are believed to have been generated by randomness in the actions of the weaving loom. We will refer to the longest wavelength deviations in tow positioning as ”handling-induced trends”.

Data for the subject 2/2 twill weave in this paper reveal handling-induced trends that are pure shear deformations (no dilation or compression, i.e., change in the separation of tows), with the shear approximately uniform over the specimen. Given this, the handling-induced trends were deduced as illustrated in figures 5(a) and 5(b), by a procedure analogous to reference period collation, but with the reference period size equal to a specimen dimension. With handling-induced trends thus defined to be uniform over the specimen, and effectively deterministic for that particular specimen, one may define stochastic deviations using an

analogue of equation 2, i.e., decompose positional variations into a systematic trend (the handling-induced trend) and stochastic deviations. The definition of the stochastic deviations for long-range data is illustrated in figure 5(c).

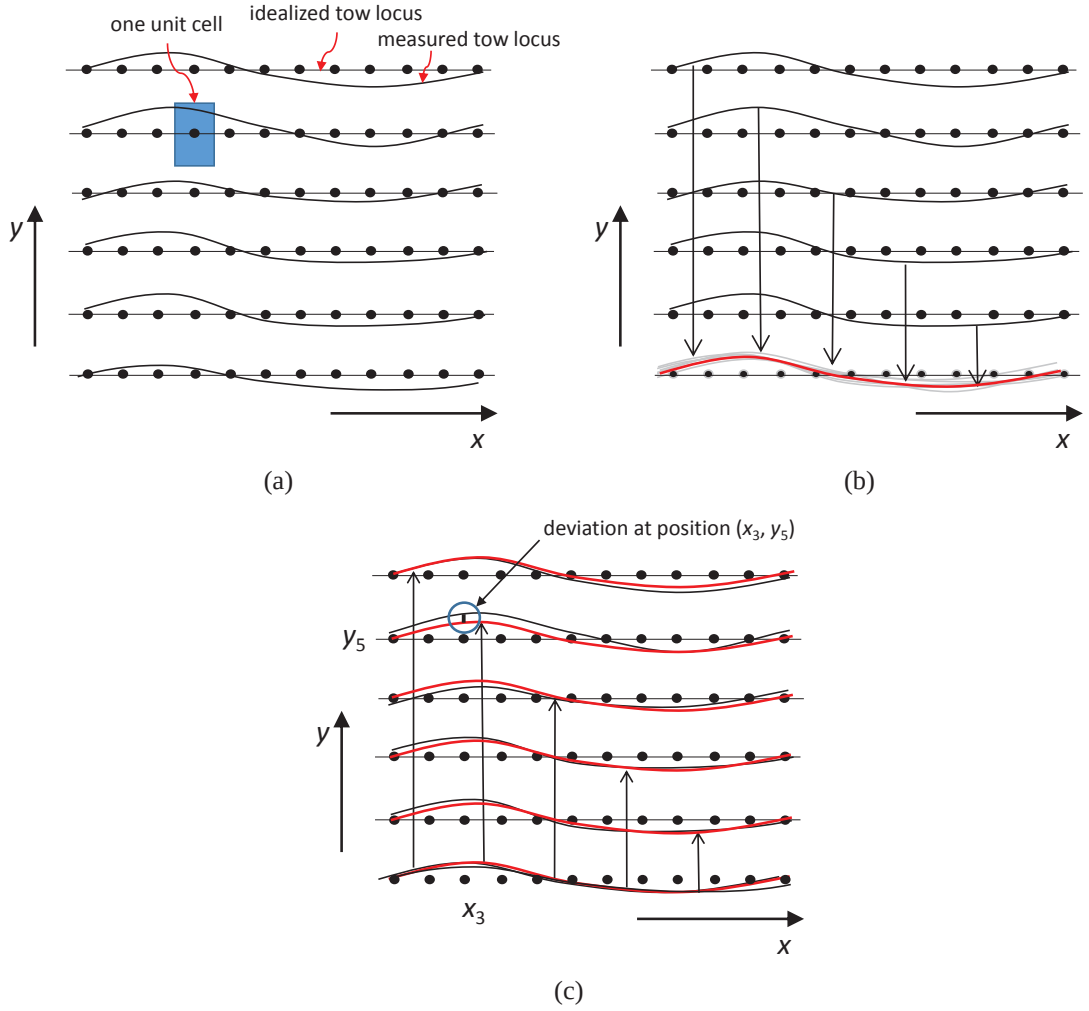


Figure 5: Handling-induced trends in long-range data. (a) Schematic of long-wavelength positional variations for warp tows found in long-range data for a specimen much larger than the unit-cell size. (b) The positional data for each tow are translated in the $y$-direction so that they approximately coincide; and the mean of the superposed data is computed as the mean handling-induced trend (red curve). (c) The deviations in tow position due to machine noise are computed translating the curve for the mean handling-induced trend back to the nominal position of any tow $j$, and the difference between the data curve for that tow and the mean handling-induced trend at any grid point $x_i$ is recorded as the deviation in the tow position at grid point ($x_i$, $y_j$).

The assignment of long-range positional deviations as ”handling-induced trends” or ”machine-induced stochastic deviations” has so far been the subjective interpretation of

long-range data for single specimens of a 3-D interlock weave [15] or one pair of specimens of a twill weave [18]. In the analysis of the 3-D interlock weave, handling-induced trends were defined to include variations in tow spacing as well as shear distortions, which appeared justified by those data [15]. Handling-induced trends might generally be expected to be stochastic, differing from specimen to specimen, unless the handling conditions were to be repeatable for some reason. Yet, curiously, in the analysis of the pair of 2/2 twill weave specimens, the handling-induced trends were found to be nearly identical for the two specimens. Many more specimens need to be analyzed before the characteristics and origin of so-called handling induced trends will be clarified. In this paper, in considering data for a single specimen, they play an analogous role in analysis to the systematic trends defined for short-range data.

*4.1.4. The data structure of deviations*

For both scales, the random deviations $\epsilon_i^{(j,t,s)}$ are computed for every data point on the grid as the departure from the mean behavior expected for that grid point for the systematic or handling-induced trends. The deviations constitute a "random field", defined over a 2-D spatial grid. Consider a tow parameter $\varepsilon \in \{\rho, z, AR, A, \theta\}$, with $\rho = y$ or $x$ for warp and weft tows, that has been evaluated for one tow genus at each grid point (figure 4). The field of deviations in $\varepsilon$ over the entire specimen can be written as a $N_i \times N_j$ random matrix **H**:

$$\mathbf{H} = \{[H^1]^T[H^2]^T...[H^{N_j}]^T\} \tag{3}$$

with

$$H^j = [\epsilon_1^j \epsilon_2^j ... \epsilon_{N_i}^j] \tag{4}$$

Each row in **H** corresponds to the tow path deviations of a single tow which are defined at equidistant positions along its length. For the example of the warp tows, presented in figure 6, the $x$-direction contains $N_i$ grid locations, corresponding to the number of columns in **H**, and the $y$-direction contains $N_j$ grid locations, corresponding to the number of rows in **H**.

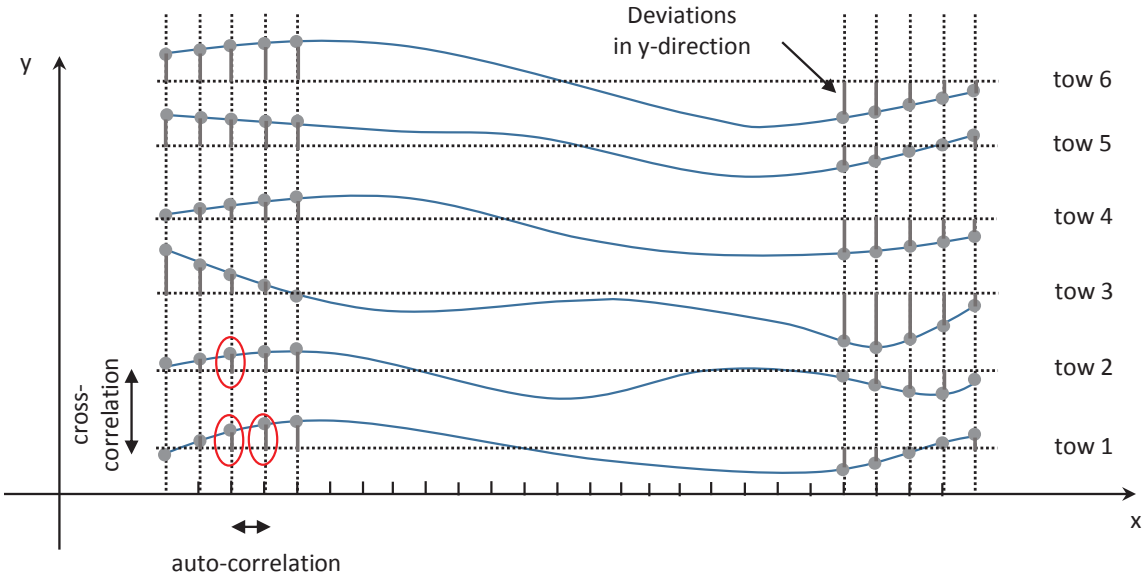


Figure 6: In-plane positional deviations of six adjacent warp tows after removal of either the systematic or handling-induced trend. Deviations are defined on a rectangular grid, with the row spacing matched to the tow spacing. The auto-correlation matrix is constructed by computing the covariance of deviations at two positions along one tow. The cross-correlation matrix is constructed by computing the covariance of deviations at two positions on different tows. The red ellipses indicate relative positions for auto-correlation and cross-correlation for a spacing of 1 unit in the correlation matrix.

### *4.1.5. Correlation information and matrix representation of correlations*

For both short-range and long-range data, correlation information is determined by computing Pearsons moment correlation coefficient for pairs of zero-mean deviation data (figure 6). In the following, we discuss the structure of correlation data involving a single tow parameter (e.g., one of the set $\{\rho, z, A, AR, \theta\}$ defined for short-range data) and a single tow type (warp or weft). Such analysis is valid when different types of tow parameters are uncorrelated. If correlations between the deviations in different tow parameters, or between warp and weft, are also considered, the data structure remains similar in form, but becomes much larger. Remarks on the size of correlation data sets appear in section 4.1.7.

First, we distinguish two categories of correlations, which recognize the fact that the magnitude of some correlations will be strongly influenced by the continuity of tows. "Auto-correlation" is determined by computing Pearson's correlation coefficient $C_{auto}(k)$ for pairs of data found for all grid points $i$ and $i'$ that have the same spacing $k = i' - i$ sampled on

the same tow, repeated for all tows of the same genus. ”Cross-correlation” is determined by computing Pearson’s correlation coefficient $C_{cross}(k, k')$ for pairs of data found at all grid points $(i, j)$ and $(i', j')$ that have the same vector spacing $(k, k') = (i, j) - (i', j')$ sampled on different tows $j$ and $j'$, repeated for all pairs of tows of the same or different genus.

The correlation matrix $R_{\mathbf{H}}$ summarizes the Pearson’s moment correlation coefficient information (auto- and cross-correlation) of any tow parameter. Most generally, one might define the correlation matrix as a square matrix of dimension $N_j N_i \times N_j N_i$, where $N_i$ is the number of grid points along a single tow (e.g., along $x$ in figure 6) and $N_j$ is the number of tows in the sample (e.g., number of grid points along $y$ in figure 6), with $N_i$ and $N_j$ taking the same values in each of an ensemble of equally sized, nominally equivalent specimens. To reflect the distinction of auto-correlations and cross-correlations, the correlation matrix $R_{\mathbf{H}}$ can be written as an array of $N_j \times N_j$ blocks with each block a submatrix $R_{jj'}$ where the subscripts identify one of the $N_F$ tows of warp or weft type in the data set (e.g. tows 1 till tow 6 in figure 6)):

$$R_{\mathbf{H}} = \begin{bmatrix} R_{11} & R_{12} & \cdots & R_{1N_F} \\ R_{21} & R_{22} & \cdots & R_{2N_F} \\ \vdots & \vdots & \cdots & \vdots \\ R_{N_F 1} & R_{N_F 2} & \cdots & R_{N_F N_F} \end{bmatrix} \tag{5}$$

Each submatrix entry is constructed from selecting one of the $N_i \times N_i$ correlation data available for tows $H_i$ and $H_j$. Submatrix $R_{jj'}$ is represented as:

$$R_{jj'} = \begin{bmatrix} r_{jj'}(x_1, x_1) & r_{jj'}(x_1, x_2) & \cdots & r_{jj'}(x_1, x_{N_i}) \\ r_{jj'}(x_2, x_1) & r_{jj'}(x_2, x_2) & \cdots & r_{jj'}(x_2, x_{N_i}) \\ \vdots & \vdots & \cdots & \vdots \\ r_{jj'}(x_{N_i}, x_1) & r_{jj'}(x_{N_i}, x_2) & \cdots & r_{jj'}(x_{N_i}, x_{N_i}) \end{bmatrix} \tag{6}$$

with $r_{jj'}(x_i, x_{i'})$ the Pearson’s correlation value between deviation values at locations $x_i$ and location $x_{i'}$ on tow $j$ and tow $j'$ respectively. Figure 6 presents in the $x$-direction one set of the pair of points needed to compute $r_{11}(x_3, x_4)$, and in the $y$-direction one set of pair

of points needed to compute $r_{12}(x_3, x_3)$. The submatrices at the diagonal of $R_{\mathbf{H}}$ thus represent the auto-correlation matrices, while the off-diagonal entries are the cross-correlations between the different tow paths.

*4.1.6. Estimated size of correlation matrices*

The correlation matrix so defined for a single tow parameter is typically very large. For example, consider a plain-weave specimen in which large-scale stochasticity is being studied and which contains 100 warp tows and 100 weft tows. For tows that are 1 mm wide, such a specimen will be $100 \times 100$ mm$^2$, a relatively modest size. Assume that grid points are located at the nominal intersections of each warp and weft pair. Then the rank of the correlation matrix for a single tow parameter, e.g., one of $\{\rho, z, A, AR, \theta\}$ for either warp or weft tows will be $10^4$. On the other hand, if a tow parameter for warp tows is assumed to be significantly correlated with the same tow parameter for weft tows, then the matrix of all possible correlations for that parameter rises to rank $2 \times 10^4$. If significant correlations exist among any two of the five tow parameters, and between any pair of warp and weft tows, then the rank of the matrix of all correlations rises again to $10^5$. Such a matrix is still comfortably manageable in computations, but, if a data-rich world generates data either for larger specimens or on a finer grid, the matrix rank may become an issue. Partly for this reason, we also consider how the representation of the correlation information can be reduced to far fewer degrees of freedom by certain assumptions about its plausible structure. The assumptions allow a second, at least equally important advantage: when certain relationships exist among correlations, statistically significant information can be obtained even from data for a single specimen.

*4.1.7. Simplified representations of correlation*

As well as assuming the absence of correlations between different tow parameters, or between warp and weft pairs, a number of other assumptions about the nature of correlations are suggested by data that have been acquired to date [49, 17, 18]:

- **Translational invariance**

It is often attractive to assume that the correlation between the deviations at a pair of grid points depends only on their vector separation $\tau_x = |x - x'|$. If this is the case, then the number of degrees of freedom in the correlation matrix, $R_{\mathbf{H}}$, is greatly reduced. In particular, all the block matrices on any diagonal of $R_{\mathbf{H}}$, whether the leading diagonal (auto-correlations) or an off-diagonal (cross-correlations) become identical; and the elements on any row within any block matrix take values that depend only on the distance of that element from the lead diagonal of the block matrix, regardless of row. The block matrix $R_{jj'}$ is now represented as:

$$R_{jj'} = \begin{bmatrix} r_{jj'}(0) & r_{jj'}(1) & \cdots & r_{jj'}(N_i - 1) \\ r_{jj'}(1) & r_{jj'}(0) & \cdots & r_{jj'}(N_i - 2) \\ \vdots & \vdots & \cdots & \vdots \\ r_{jj'}(N_i - 1) & r_{jj'}(N_i - 2) & \cdots & r_{jj'}(0) \end{bmatrix} \tag{7}$$

with $r_{jj'}(k)$ the Pearson's correlation value between deviation values of tow $j$ and tow $j'$ which are separated by a vector $k\delta$ over the grid ($k = 0..N_i - 1$).

- **Series expansions and correlation lengths**

  Further simplification of the correlation data matrix can be achieved by analyzing the manner in which correlations decay as the distance between two grid points increases, i.e., the rate of decay of the magnitude of elements of any of the block matrices, $R_{jj'}$, with distance of the element from the lead diagonal of $R_{\mathbf{H}}$. The most complete analysis of this decay is performed using a Series Expansion method. The Series Expansion method uses a modest number of degrees of freedom to describe the decay. In the simplest possible analysis, the decay is defined by a single parameter, such as the correlation length. Both the Series Expansion method and the definition of the correlation length are described fully in section 5.

The question of how the functions $C_{auto}(k)$ and $C_{cross}(k, k')$ depend on the point separations $k$ and $k'$, and whether cross-correlations $C_{cross}(k, k')$ are significant, determine the preferred

method and the complexity of generating virtual specimens.

### *4.2. Illustrative data from a 2/2 twill weave*

#### *4.2.1. Material description*

Data for a 2/2 twill woven carbon fibre Hexcel fabric (G0986 injectex) [51], impregnated with epoxy resin using a resin transfer moulding (RTM) production process [17], show qualitative characteristics that prove to be similar to those found for a number of other weaves (3-D interlock weaves) for which data have been analyzed to date. In the twill weave, each unit cell of the reinforcement consists of four equally spaced warp and weft tows with periodic lengths of the warp (x-axis) and weft (y-axis) tows that are nominally identical: $\lambda_x = \lambda_y$=11.43 mm. Warp tows are represented by one genus and weft tows as a second. Figure 3 shows a numerical model of the textile geometry.

#### *4.2.2. Short-range information*

Short-range variations are identified in [17] from a seven-ply sample of dimensions comparable to one unit cell using laboratory X-ray micro-CT. Information about the tow path centroids $(\rho, z)$ with $\rho$=y for the warp tows and $\rho$=x for the weft tows, tow aspect ratio *AR*, tow area *A* and tow orientation $\theta$ in cross-section are extracted. Statistical information ($\sigma$, $\xi_{auto}$) of all tow path parameters, combined from all seven plies, are given in tables 1 and 2.

Auto-correlations $C_{auto}(k)$ in the short-range data are characterized by a single scalar parameter, the correlation length $\xi$, which "measures the distance of two different stochastic field locations over which the correlation between the respective random variables approaches zero or a practically very small value" [3]. The value of $\xi$ is determined using linear regression of only the first five *k* values, because higher *k* values are noisy due to the small specimen size that can be analyzed by micro-CT. Cross-correlations in the short-range data are found by statistical analysis to be negligible, whether between tows of the same or different genuses [13].

*4.2.3. Long-range information*

The short-range data for tow paths hint at possible long-range correlations for the in-plane component of the positional deviations for any tow. Additional data were therefore acquired for the deviation of the centroid of each tow, sampled by optical imaging for a few locations per unit cell position in large one-ply samples of size $13 \times 13$ unit cells [18], from which a region of $10 \times 10$ unit cells is inspected. The long-range in-plane deviations were expressed in terms of their standard deviations and the correlation lengths $\xi$ for decay along the tow and between tows (tables 1 and 2). The correlation length was evaluated for warp tows by fitting an exponential correlation function $C_{exp} = \exp\left(-\frac{\tau_x}{\xi}\right)$ to the data, while the correlation length between weft tows was evaluated by fitting a squared exponential correlation function $C_{sq,exp} = \exp\left(-\frac{\tau_x^2}{\xi^2}\right)$ to the data.

*4.2.4. Multi-scale character implied by systematic trends and correlation information*

Systematic trends in short-range data, whether for the out-of-plane centroid coordinate $z$ (figure 7(a)), the aspect ratio $AR$ (figure 7(c)), or the cross-sectional area $A$ (figure 7(d)), exhibit periodic variations consistent with the known locations of crossovers between warp and weft tows. In contrast, systematic trends in the in-plane centroid position $\rho = y$ or $\rho = x$ for the long-range data show aperiodic behavior with spatial wavelength approximating the specimen dimensions (figure 7(b)). Because the wavelength approximates the specimen dimensions, we interpret the systematic trends in long-range data as the result of handling of the fabric after its removal from the loom, i.e., handling-induced trends.

In contrast to the systematic trends, the deviations in both the long-range and short-range data we interpret as generated during fabrication of the textile on the loom, arising from chatter in the motion of loom components. A similar distinction was suggested by analysis of statistical data for 3-D interlock weaves [15]. The rate of decay of auto-correlations $C_{auto}(k)$ with point separation $k$ is substantially different for short-range and long-range data, indicating the probable presence of distinct mechanisms for their origin.

As illustrated by the data for the 2/2 twill weave and for data for a 3-D interlock composite [49], the number of parameters needed to describe deviations at the meso-scale (unit-

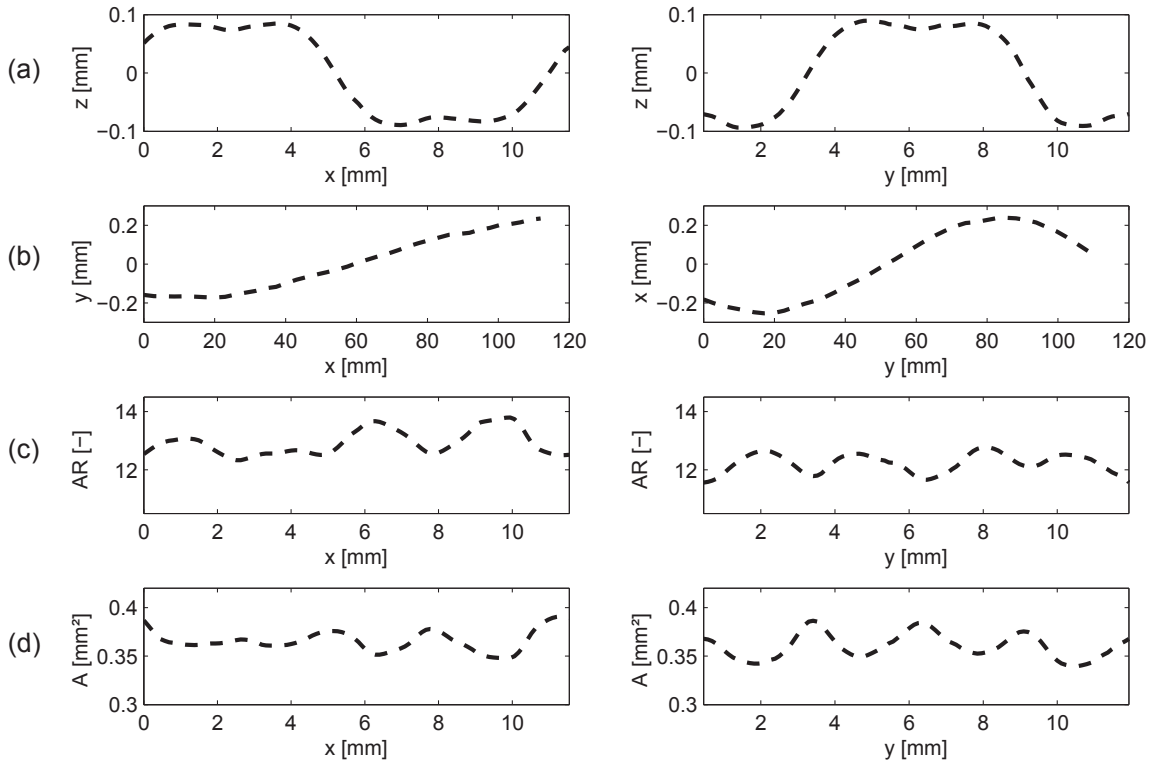


Figure 7: Periodic average and handling trends after translation of all tows per tow path parameter to their reference period, with the warp genuses defined along x-axis and the weft genuses along y-axis. Periodic trends are represented for one unit cell distance, while the handling effect is shown over a distance of ten unit cells.

cell scale) is usually greater than needed at the macro-scale. For example, the 2/2 twill composite is represented by five parameters at the meso-scale $\{z, A, AR, \theta\}$ and one at the macro-scale $\{\rho\}$. Positional variations and shape distortions of tows at the unit-cell scale, where tows are influenced by crossovers with variable spacing, are more complex than the gradual drift in tow position that manifests over many unit cells.

### *4.2.5. Summary of statistical data*

Standard deviations and correlation lengths for the short-range deviations and long-range deviations (in-plane position coordinate only) are reported in tables 1 and 2. These, as well as more complete records of correlations, will be used in a multi-scale strategy for generating virtual specimens.

## 5. Generating instantiations of stochastic textile reinforcement using multi-scale modelling (step 2)

### *5.1. Generation strategy*

The strategy for generating instantiations of stochastic textiles, or stochastic virtual specimens, fits within the overarching strategy depicted in figure 2: the reconstruction step replicates target statistics that have been determined by experiment to create virtual specimens that can be used in predictions of performance and lifetime. The reconstruction process yields ensembles of instantiations of stochastic virtual specimens, by executing the following steps:

1. A system of four discrete rectangular 2-D lattices is constructed for generating long-range positional variations and short-range positional variations for warp and weft tows, which is the same as were used to analyse data in section 4.1.1 but is not necessary. In general, where archived statistics are being used to calibrate the virtual specimen generator, the grid used to analyse data may not even be known. It is also convenient to define the grid locations of the long-range lattice to coincide with a subset of the grid locations for the short-range variations. However, the grid spacing in the grid for generating short-range variations should be equal to or smaller than the shortest correlation length identified by experimental analysis; and, if the effects of all components of long-range deviations are to be analyzed using virtual specimens in virtual tests, then the overall dimensions of the virtual specimen generated (i.e., the total number of grid points) should exceed the longest correlation length iden-

Table 1: Standard deviation of the tow path parameters from the short-range [17] and long-range characterisation [18], respectively indicated by *sr* and *lr*.

| | $\sigma_x^{sr}$ [mm] | $\sigma_y^{sr}$ [mm] | $\sigma_z^{sr}$ [mm] | $\sigma_{AR}^{sr}$ [-] | $\sigma_A^{sr}$ [mm$^2$] | $\sigma_\theta^{sr}$ [°] | $\sigma_x^{lr}$ [mm] | $\sigma_y^{lr}$ [mm] |
|---|---|---|---|---|---|---|---|---|
| $\sigma^{warp}$ | - | 0.113 | 0.014 | 1.774 | 0.023 | 0.797 | - | 0.106 |
| $\sigma^{weft}$ | 0.063 | - | 0.015 | 1.440 | 0.024 | 0.833 | 0.615 | - |

Table 2: Correlation lengths of the tow path parameters from the short-range [17] and long-range characterisation [18], respectively indicated by *sr* and *lr*. Only for the in-plane position a cross-correlation length is defined.

| | $\xi_x^{sr}$ [mm] | $\xi_y^{sr}$ [mm] | $\xi_z^{sr}$ [mm] | $\xi_{AR}^{sr}$ [mm] | $\xi_A^{sr}$ [mm] | $\xi_\theta^{sr}$ [mm] | $\xi_x^{lr}$ [mm] | $\xi_y^{lr}$ [mm] |
|---|---|---|---|---|---|---|---|---|
| $\xi_{auto}^{warp}$ | - | 22.89 | 1.78 | 7.26 | 2.53 | 4.56 | - | 114.89 |
| $\xi_{cross}^{warp}$ | - | - | - | - | - | - | - | 4.49 |
| $\xi_{auto}^{weft}$ | 9.42 | - | 1.62 | 5.48 | 1.01 | 3.49 | 52.89 | - |
| $\xi_{cross}^{weft}$ | - | - | - | - | - | - | 13.16 | - |

tified by experimental analysis. The following steps are then iterated for each tow characteristic.

2. Long-range, handling-induced trends (figure 5) are generated for warp and weft tows at the grid locations of the sparser grid for long-range variations. Values at the grid locations of the finer grid for short-range variations are then generated by interpolation.

3. Short-range, deterministic trends are generated for warp and weft tows at the grid locations of the finer grid for short-range variations. Since the virtual specimen is generally much larger than one unit cell, whereas the short-range, deterministic trends are recorded over a single reference period, the short-range, deterministic trends for the whole virtual specimen must be generated using the reverse of the process of reference period collation (figure 4) [40]: values at any grid point are set equal to the value at the corresponding point in the reference period, which is shifted from the grid point in question by a lattice vector, $k/N_{j,y}\mathbf{a} + l/N_{j,x}\mathbf{b}$, where $k$ and $l$ integers (section 4.1.2).

4. The long-range handling-induced trends and the short-range deterministic trends are combined at all locations on the finer grid by linear superposition. Linear superposition is valid because the spatial gradient in the long-range handling-induced trends is generally small over gauge lengths commensurate with the unit cell and therefore the long-range handling-induced trends will not have influenced the deduction of short-

range deterministic trends from experimental data.

5. Long-range stochastic deviations are generated at all locations of the sparser grid using Monte Carlo Markov Chain methods or Series Expansion techniques. Values of long-range stochastic deviations are then generated at all locations on the finer grid by interpolation.
6. Short-range stochastic deviations are generated at all locations of the finer grid using Monte Carlo Markov Chain methods.
7. The long-range deviations and the short-range deviations are combined at all locations on the finer grid by linear superposition. The validity of using linear superposition rests on whether the short-range and long-range deviations are uncorrelated. Because the characteristic wavelength of significant spectral components of the short-range deviations tends to be less than the shortest characteristic wavelength of long-range deviations, their correlation is likely to be weak. However, proof of this assumption awaits richer data sets.
8. The deterministic trends resulting from step (4) are combined with the stochastic deviations resulting from step (7) to create the complete specification of one tow characteristic throughout a single stochastic virtual specimen.
9. Steps (2) through (8) are repeated for all tow characteristics, and for both warp and weft tows, to create a single virtual specimen.
10. Steps (2) through (9) are iterated to generate an ensemble of stochastic virtual specimens.

The above scheme implicitly assumes that deviations on tows of different type (warp and weft) are uncorrelated. This is a valid assumption for a number of data sets gathered to date. Elaborations of the process to treat correlations between tows of different type appear in [52].

We will illustrate this procedure, for a single ply of fabric with tow parameters consisting of the set $\{\rho, z, A, AR, \theta\}$. However, the procedure would remain the same for any type of periodic textile, including 3-D weaves, except that, if a larger numbers of tow genuses were

present, the procedure would be based on an appropriately enriched lattice.

*5.2. Reconstruction algorithms*

A number of algorithms have been developed to solve the reconstruction problem, i.e., to generate instantiations of the stochastic textile reinforcement whose statistics match those derived from experimental data (standard deviation and correlation data). The algorithms were all developed to take advantage of the fact that statistical data for textiles tend, like the textiles themselves, to be highly anisotropic, usually with slow variations along the length of tows but rapid variations in the orthogonal direction. But even given this common condition, different algorithms are warranted depending on the richness of available data and differences in the magnitudes of certain correlations.

- A Markov chain algorithm deals with either short-range or long-range deviations along a single tow when auto-correlations decay in a simple manner or the experimental data are relatively sparse.

- A Series Expansion algorithm deals with either short-range or long-range deviations along a single tow when auto-correlations exhibit more complex behavior and the experimental data are relatively rich.

- A combination of Fourier analysis and the Markov Chain algorithm and a random walk model deals with long-range deviations data in which cross-correlations are strong and complex (not well represented by a single correlation length), auto-correlations are strong but relatively simple (can be represented by a single correlation length for each amplitude and phase), and data are relatively rich.

- A matrix cross-correlated Series Expansion method deals with either short-range or long-range deviations when deviations exhibit significant cross-correlations between tows and identical, relatively complex auto-correlation behavior along each tow, and

data are relatively rich. [1].

In the following, we briefly describe the Markov Chain algorithm [40, 41, 17], the Series Expansion technique [38, 14], and the Fourier Transform method [15]. In section 5.4, we illustrate the advantages of the first two reconstruction algorithms (Markov Chain & Series Expansion) by their application to data from the 2/2 twill weave described in section 4.2.

### *5.2.1. The Monte Carlo Markov Chain method for reconstructing auto-correlated deviations*

The Monte Carlo Markov Chain method offers a simple and fast method of reconstructing tow parameters for textile structures [40]. The algorithm is applicable when cross-correlations of deviations on different tows are negligible. The Markov Chain generator acts for each tow parameter separately and is calibrated by the corresponding experimentally determined standard deviation and auto-correlation length.

First, the deviations of the considered parameter $\epsilon$ are discretised on an interval with grid spacing $a$ ($a$ is chosen independently from lattice spacing $\nu$) and number of intervals $2m+1$: $\{-ma, -(m-1)a, ..., 0, ..., (m-1)a, ma\}$ that satisfies the relation $ma = 3\sigma_\epsilon$. The parameter $m$ must be chosen not too low to avoid discontinuity errors due to the discreteness of the representation and not too high to minimize computational time. The probability of occurrence of the discrete values of $\epsilon$ constitutes the distribution vector $P_i^\epsilon$ for location $i$:

$$P_i^\epsilon = \left[ \begin{array}{ccccccc} p_m^{(i)} & p_{m-1}^{(i)} & \dots & p_0^{(i)} & \dots & p_{-m+1}^{(i)} & p_{-m}^{(i)} \end{array} \right]^T \tag{8}$$

with $T$ denoting the transpose operation. The Markov process generates the distribution vector $P_{i+1}^\epsilon$ of the particular parameter $\epsilon$ at the next grid location $i+1$ using the probability transition matrix $A_{trans}^\epsilon$:

$$P_{i+1}^\epsilon = A_{trans}^\epsilon P_i^\epsilon \tag{9}$$

[1] The requirement of identical auto-correlation behaviour is not mandatory, but considerably simplifies the analysis

To begin, a tri-diagonal probability transition matrix (PTM) is constructed containing two independent parameters $\alpha$ and $\beta$ and a third dependent parameter $\gamma = 1 - \alpha - \beta$:

$$A_{trans,0} = \begin{bmatrix} \alpha & \gamma & 0 & . & & & & & . & 0 \\ 1-\alpha & \alpha & \gamma & 0 & . & & & & & . \\ 0 & \beta & \alpha & . & . & . & & & & \\ . & 0 & . & . & \gamma & 0 & . & & & \\ & . & . & \beta & \alpha & \frac{1-\alpha}{2} & 0 & . & & \\ & & . & 0 & \beta & \alpha & \beta & 0 & . & \\ & & & . & 0 & \frac{1-\alpha}{2} & \alpha & \beta & . & . \\ & & & & . & 0 & \gamma & . & . & 0 \\ & & & & & . & . & . & \alpha & \beta \\ . & & & & & & & 0 & \gamma & \alpha \\ 0 & . & & & & & & . & 0 & \gamma \end{bmatrix} \begin{matrix} . & 0 \\ & . \\ & \\ & \\ & \\ & \\ & \\ & \\ \beta & 0 \\ \alpha & 1-\alpha \\ \gamma & \alpha \end{matrix} \tag{10}$$

The parameter $\alpha$ is given an arbitrary fixed value of 0.9, while $\beta$ is chosen to match the target standard deviation $\sigma^{\epsilon}$ (figure 8(a)): the more $\beta$ exceeds $\gamma$, the more likely is each application of the PTM to move the value of $\epsilon$ away from its mean. Next, the target correlation length (information of the nearest neighbour: $k$=1) is matched by constructing the new PTM $A^{\epsilon}_{trans} = A^{N_A}_{trans,0}$, which is the iterative re-application of the tri-diagonal form $A_{trans,0}$. The parameter $N_A$ is calibrated from the graph shown in figure 8(b), which was built for the choice of $\alpha = 0.9$, $m$=10 and a particular choice of $\beta$.

The Markovian procedure is the core computation within the Monte Carlo based scheme which is repeated for all parameters [40], with a different (2$m$+1) by (2$m$+1) probability transition matrix $A^{\epsilon}_{trans}$ for each tow parameter. A sequence of deviation values along a tow is initiated by mapping a uniform random number onto the cumulative probability distribution of the vector $P$ of equation 8 that represents the expected distribution of $A_{trans}$. Subsequent values in the sequence are generated by mapping further random numbers onto the row of $A_{trans}$ that corresponds to the value of the deviation $\epsilon$ at the previous grid location.

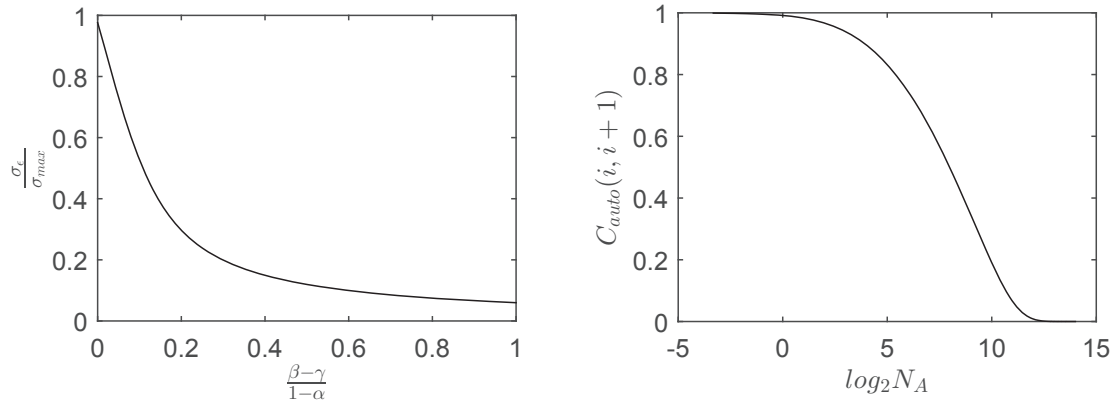


(a) (b)

Figure 8: Graphs used to calibrate the probability transition matrix: (a) ratio $\sigma_\epsilon/\sigma_{max}$, where $\sigma_{max}$ is the variance generated by the PTM $A_{trans,0}$ in the case $\beta = \gamma$ and (b) the number $N_A$ of iterative application of $A_{trans,0}$ required to reproduce the target correlation length.

The generated deviations possess high-amplitude long-range wavelength fluctuations, according to the auto-correlation length, combined with low-amplitude short-range wavelength variations. The latter are numerical noise associated with the discreteness of the Markov Chain and are not observed in experiments. A post-processing smoothing operation reduces the short-range noise without affecting the statistics of the deviations to an unacceptable degree. The smoothing is a modified version of the moving box average that conserves the standard deviation [40]. However, when deviations with different signs are present in the averaging interval, the conventional moving averaging rule must be applied which does not conserve the standard deviation. Deviation values are typically smoothed using information over ±2 neighbouring grid points.

### *5.2.2. The cross-correlated Karhunen-Loève Series Expansion technique for reconstructing auto- and cross-correlated deviations*

The K-L Series Expansion [11, 53] is a common technique to discretise and generate realisations of finite deviations represented as *random fields*. This method involves the spectral representation of the correlation matrix $R_{\mathbf{H}}$, described in section 4.1.5, in a form of principal component analysis [54].

This section describes (1) the general case, in which different tows of the same type may have different auto-correlation behaviour and cross-correlation between different tows of the same type are not necessarily spatially homogeneous (e.g., for warp tows, cross-correlations for a pair of points that have the same $x$-coordinate on two different tows may vary when $x$ is varied), and (2) a simplified approach, for a specimen in which all different tows of the same type share the same auto-correlation behaviour and cross-correlations between different tows of the same type are spatially homogeneous, represented by a single coefficient (e.g., for warp tows, cross-correlations for a pair of points that have the same $x$-coordinate on two different warp tows are independent of $x$). The latter method is especially interesting for standard weave structures.

Both algorithms are calibrated with the experimental standard deviation, and auto-correlation and cross-correlation statistics. Truncation of the principal component analysis in each correlation direction is different and related to how rapidly the variations occur: rapid variations in the direction normal to the tows and a much slower variation along the tow path, is the common case for long tows of continuous fibres.

In the general case (algorithm 1), a single realisation of a set of zero-mean tow path deviations $\{\tilde{\epsilon}_i^j, i = 1..N_i, j = 1..N_j\}$ in the same format as $\mathbf{H}$ and represented by $\tilde{\mathbf{H}}$, is generated by performing the Karhunen-Loève Series Expansion [55, 11, 53]:

$$\tilde{\mathbf{H}}(x) = \sum_{z=1}^{N_j N_i} \sqrt{\lambda_z}\eta_z\phi_z(x) \tag{11}$$

with $\{\eta_z, z = 1..N_jN_i\}$ a set of centred orthonormal random variables and $\{\lambda_z, \phi_z, z = 1..N_jN_i\}$ the eigenvalues and eigenvectors obtained by solving the eigenequation of $R_{\mathbf{H}}$:

$$R_{\mathbf{H}}\Phi = \Lambda\Phi \tag{12}$$

with $\Lambda$ a diagonal matrix with the $N_jN_i$ eigenvectors on its diagonal and *Phi* the eigenvector matrix that has as dimensions $N_jN_i \times N_jN_i$. In practice, a truncation of the series is per-

formed. The number of K-L terms in the series is defined by ordering the eigenvalues in a descending series and considering only the larger eigenvalues, which correspond to the most influential variations. The number of eigenvalues retained is determined by testing for adequate representation of the experimentally measured randomness. Since these generated set of deviations are standardised Gaussian random fields, a normalisation step to the experimental standard deviation should be performed which can be different for each individual field that represent deviations of a single tow path since the standard deviation is different for tows belonging to a different genus: $H^j\sigma_j (j = 1..N_j)$.

The general approach requires the solution of a high-dimensional eigenvalue problem of the correlation matrix $R_{\mathbf{H}}$ (order $N_i N_j$). Vořechovský (algorithm 2) proposes a significant reduction in this dimension for a set of deviations $\{\tilde{\epsilon}_i^j , i = 1..N_i , j = 1..N_j\}$, in which the auto-correlation and cross-correlation structures are treated as separable: the individual 1-D fields (tow paths) share the same auto-correlation, assumed to depend only on the separation of points in the tow direction, while the cross-correlations between the 1-D fields (tow paths) are represented by the so called "cross-correlation coefficients". For each certain distance between two tows, a different cross-correlation coefficient is computed (total $N_j - 1$ scalars) by using the Pearson's correlation coefficient $C_{cross}(k, k')$ for pairs of data found at all grid points $(i, j)$ and $(i + 1, j')$, where $j$ and $j'$ have a fixed spacing and with a vector spacing $(k, k') = (i, j) - (i + 1, j')$ repeated for all pairs of points along each set of two tows (figure 6). The methodology requires only the information of this one scalar to reconstruct its cross-correlation structure by multiplication of the subject cross-correlation coefficient with the entire auto-correlation structure. This approach with cross-correlation coefficient depending only on the separation of two tows, is specifically valid in case the auto-correlation is the same for the tows for which the cross-correlation is evaluated, with the auto-correlation only depending on the separation of points. Under these conditions, the approach yields identically good results as if the generation of deviations would be performed with the general correlation matrix $R_{\mathbf{H}}$ [38].

In summary, the correlation information of $R_{\mathbf{H}}$ can be fully represented by two separate correlation matrices: an auto-correlation matrix $R_A$ of order $N_i$, which is identical for all individual tow paths, and a cross-correlation matrix $R_C$ of order $N_j$ which describes all the cross-correlation coefficients between the different tow paths. Both matrices are constructed similarly as for the submatrix $R_{H_jH_j}$ in section 4.1.5 while assuming that the correlation between the deviations at a pair of grid points depends only on their vector separation $\tau_x = |x - x'|$ (section 4.1.7). Instead of performing a normalisation of the generated random fields to the experimental standard deviation, the auto-correlation matrix is already multiplied by the square of the standard deviation before performing its eigendecomposition. Such an approach can save considerable computational effort for large $R_{\mathbf{H}}$ since now the eigendecomposition of the auto-correlation matrix and cross-correlation matrix, which are of much smaller dimensions, can be performed separately.

The approach of Vořechovský based on $R_A$ and $R_C$ and using the Karhunen-Loève Series Expansion consists of subsequent steps to acquire $N_{sim}$ realisations of cross-correlated tow paths ($10^4$ specimens) [14, 38]:

1. Perform eigendecomposition of the auto-correlation matrix $R_A = [\Phi^A][\Lambda^A][\Phi^A]^T$ and apply truncation: $\lambda_i^A$, $\phi_i^A(x)$ with $i = 1..N_{var}$ ($N_{var} \leq N_i$).
   Truncation is applied by ordering the eigenvalues $\lambda_i^A$ in a descending series and considering only the $N_{var}$ larger eigenvalues $\lambda_i^A$ and corresponding eigenvectors $\phi_i^A(x)$ that capture most of the randomness.
2. Perform eigendecomposition of the cross-correlation matrix $R_C = [\Phi^C][\Lambda^C][\Phi^C]^T$ and apply truncation: $\lambda_i^C$, $\phi_i^C(x)$ with $i = 1..N_{f,r}$ ($N_{f,r} \leq N_j$).
   Truncation is applied by ordering the eigenvalues $\lambda_i^C$ in a descending series and considering only the $N_{f,r}$ larger eigenvalues $\lambda_i^C$ and corresponding eigenvectors $\phi_i^C(x)$ that capture most of the randomness.
3. Generate $N_r \times N_{sim}$ ($N_r = N_{var} \cdot N_{f,r}$) Gaussian uncorrelated random variables $\eta_r$ using Latin Hypercube Sampling (LHS).

4. Construct the block sample matrix $\chi^D$ ($N_r \times N_{sim}$):

$$\chi^D = [\phi^D][\Lambda^D]^{1/2}\eta_r \tag{13}$$

with $\chi^D$ consisting of $j$ blocks ($j = 1..N_j$): $\chi^D = \begin{bmatrix} [\chi_1^D]^T & [\chi_2^D]^T & \cdots & [\chi_{N_F}^D]^T \end{bmatrix}^T$ where the elements of each block deliver the $N_{var}$ standard Gaussian uncorrelated random variables used in the next step to generate $\tilde{H}_j(x)$, while the different blocks are mutually cross-correlated.

5. Simulate a single realisation of the deviations of each tow path $H_j$ and apply truncation [38]:

$$\tilde{H}_j(x) = \sum_{i=1}^{N_{var}} \sqrt{\lambda_i^A}\chi_{j,i}^D\phi_i^A(x) \tag{14}$$

Combination of the individual tow path realisations results in $\tilde{\mathbf{H}}(x)$ ($N_r \times N_{sim}$).

This approach expands all cross-correlated fields (tow paths) within a single specimen using the same spectrum of eigenvalues $\lambda_i^A$ and -vectors $\phi_i^A(x)$, deduced from the auto-correlation matrix, but the sets of uncorrelated random variables used for the expansion of each field are now cross-correlated with neighbouring fields.

The introduction of cross-correlation for the random variables in step 4 is crucial in the procedure and reproduces the cross-correlation information between the different $N_j$ tow paths using the matrix decomposition method of equation 13. The eigenvalues $\lambda^D$ and -vectors $\phi^D$ in equation 13 are solutions of the eigenvalue problem (similar as equation 12) of a block cross-correlation matrix $D$ of dimension $N_{var}N_{f,r} \times N_{var}N_{f,r}$:

$$D = \begin{bmatrix} I & C_{1,2}I & C_{1,3}I & \cdots & C_{1,N_F}I \\ \vdots & I & C_{2,3}I & \cdots & C_{2,N_F}I \\ \vdots & \vdots & I & \cdots & C_{3,N_F}I \\ \vdots & sym & \cdots & \ddots & \vdots \\ \cdots & \cdots & \cdots & \cdots & I \end{bmatrix} \tag{15}$$

This matrix possesses squared blocks ($N_{var} \cdot N_{var}$) of unit matrices on its diagonal, while off-diagonal blocks represent the cross-correlation between each two sets of random fields using the entries of the cross-correlation matrix $R_C$.

In addition to this framework, Vořechovský proposes an improvement of the accuracy of the simulated auto-correlation by (i) applying correlation control techniques [56] and (ii) the anticipation of additional grid locations on the sides for each field. This first operation encounters the problem of spurious correlation which is sometimes introduced along the random variables $\chi^D_{j,i}$ of a single field. The effect of such techniques needs to be assessed for each new topology to determine if this computational expensive procedure is required or not. Furthermore, extra side points can be considered in the case disturbances are present in the generated values at the edges of the field.

### *5.2.3. The Fourier Transform method for reconstructing auto- and cross-correlated deviations*

In many cases, long-range deviations of a tow parameter are expected to be statistically homogeneous over a sample, but anisotropic, having rapid and complex variations in the direction perpendicular to the tow direction and slow variations parallel to the tow direction. For such cases, a method of Fourier analysis was developed that takes advantage of the anisotropy to yield a relatively simple formulation with rapid execution [15].

Experimental data are of the type illustrated in section 4.2 for long-range variations for the twill weave, i.e., they consist of a 2-D grid of stochastic position values for one type of tow (warp or weft). The data are partitioned into a sequence of scan lines, oriented perpendicular to the nominal tow direction (figure 9). The position values along each scan line are subjected to discrete Fourier analysis, yielding an amplitude and phase value for each frequency in a finite series. When the Fourier spectra for all scan lines are assembled, variations of the amplitude and phase of each spectral component along the nominal tow direction can be collated. For each amplitude, the variation along the tow direction is characterized by its standard deviation and correlation length. For each phase, the variation along the tow direction is modeled as a random walk and characterized by a mean path

length. Thus the stochastic data for a given tow parameter are fully characterized by the standard deviation and correlation length of the amplitude, and the random walk mean path length, for each of a series of Fourier wavelengths. The number of Fourier components depends on the specimen size, but is typically 10, to order of magnitude.

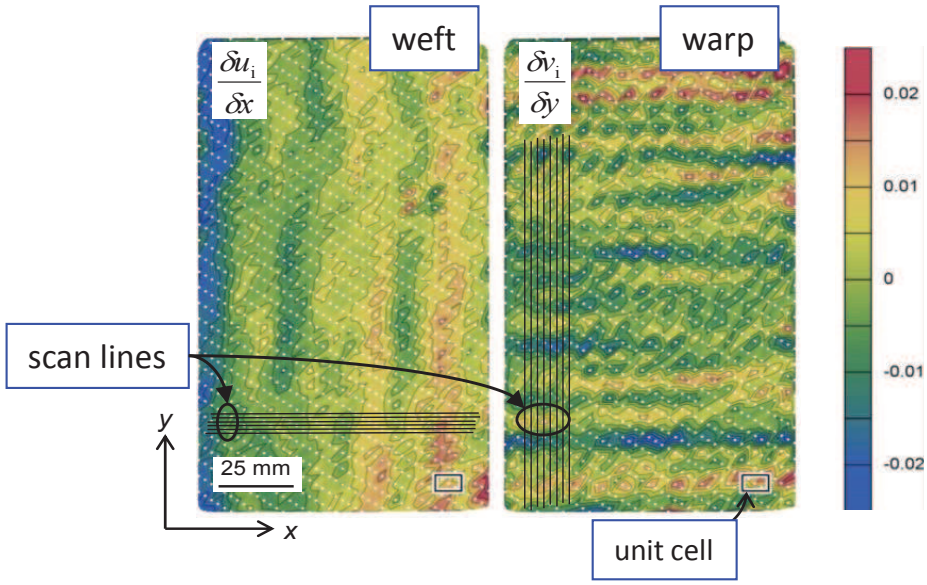


Figure 9: Data for positional variations of warp and weft tows in a 3-D angle interlock weave (from [15]). The images show spatial derivatives of the lateral positional variations of tows, which are dimensionless. Some representative scan lines are indicated (but not all), along which FFT analyses of the positional variations were performed. Variations of the Fourier coefficients from one scan line to the next can be described quite simply.

The generation of instantiations of the full 2-D field is executed by forming inverse Fourier transforms along each of the scan lines. The amplitude for each Fourier component to be used at each scan line in the sequence of scan lines is generated using the Markov Chain procedure of section 5.2.1, with the transition matrix $A_{trans}$ calibrated by the experimentally determined standard deviation and correlation length for that amplitude. The phase for each Fourier component to be used at each scan line in the sequence of scan lines is generated by a random walk generator, calibrated by the experimentally determined mean path length for that phase.

When the Fourier analysis method was applied to data for 3-D interlock weaves, handling-induced deformation was revealed, similar to that described in section 4.2 for data for the

twill weave. A simple way of filtering such long-wavelength trends out of the Fourier analysis was demonstrated: if the Fourier analysis is applied to the spatial derivative of the position field, rather than to the field itself, the Fourier spectra are dominated by the shorter-wavelength spatial variations; the long-wavelength handling trends are filtered out.

### *5.3. Further remarks on the integration of scales*

Because different numbers of parameters and grids with different spacings are used to represent short-range and long-range stochastic behavior, the short-range and long-range characteristics of instantiations (virtual specimens) are most conveniently generated separately. The instantiations must then be integrated onto a common grid. The integration of the short-range and long-range deviations for parameter $\varepsilon$, denoted $\epsilon^{sr}$ and $\epsilon^{lr}$, respectively, can be achieved by simple superposition and numerical interpolation provided the short-range and long-range deviations are statistically independent. This integration of long-range deviations and short-range deviations, as described in steps (1) to (10) in section 5.1, must deal with the fact that complete 3-D descriptions of the tow path are available at the unit-cell scale, whereas incomplete 2-D surface information is available at the sub-component scale, typically one or a few points per unit cell and often restricted to in-plane positional variations. Where data on long-range variations are absent, the entire virtual specimen will be generated using short-range variations only. Further, when the two scales are combined onto a dense grid spanning the macro-scale, the number of degrees of freedom (DOFs) in the entire composite model becomes very large. However, the potential benefits of high-fidelity studies of the effects of stochastic microstructure on sub-components may justify very large computations.

### *5.4. Application to a woven textile composite*

#### *5.4.1. Overview*

Virtual models are generated for the 2/2 twill woven textile spanning a region of ten by ten unit cells, and thus containing each forty warp and forty weft tows. The model is representative of one ply within a laminate. Each tow is discretised in 320 equidistant points

such that the information of one unit cell is defined over a grid of thirty-two points. This procedure is shown in figure 10 for the out-of-plane centroid coordinate. A total of $4 \times 10^4$ warp and weft tows, with lengths equal to ten times the unit cell periods, are simulated to create $10^3$ virtual specimens. Comparison with the experimental target values is performed by analysing histograms of the statistics and evaluating a normalised difference $\Delta$ from the target values, defined as

$$\Delta = |\frac{\upsilon^{exp} - \upsilon^{sim}}{\upsilon^{exp}}| \cdot 100\% \tag{16}$$

with $\upsilon$ equal to the standard deviation, auto-correlation length or cross-correlation length.

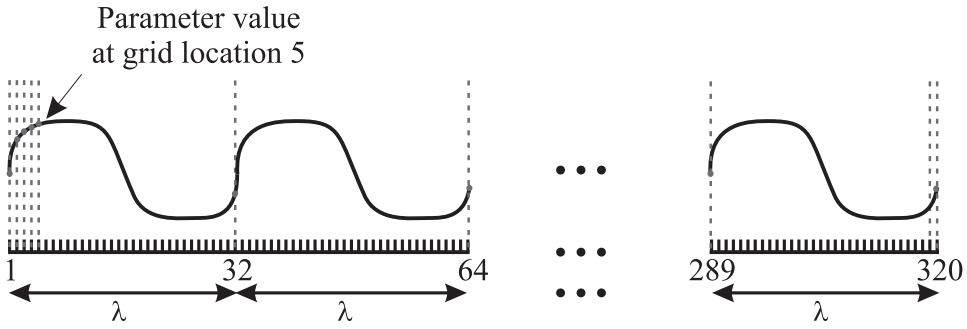


Figure 10: Procedure of generating a discretised tow representation, demonstrated for the out-of-plane centroid position.

The modelling procedure is based on several assumptions:

- Deviations are assumed to be normally distributed
- The cross-section of a tow is approximated by an ellipse
- Short-range and long-range deviations are statistically independent of each other
- In-plane long-range deviations, characterised from a single-ply sample, are also representative of a multi-ply sample
- Short-range deviations do not have any repetitive long-range effect exceeding the unit cell size

The first and second assumptions are validated by the limited experimental data for the twill weave, as well as data for 3-D woven ceramic matrix composites [49, 40, 15, 46]. Validation for other materials, and for richer databases of the materials studied so far, awaits future experiments. A more realistic geometrical shape of a tow in cross-section can be acquired using moment analysis (see appendix A of [17]) or splines [57]. The lack of cross-correlation between short-range parameters and the long-range in-plane centroid permits the independent generation of short- and long-range deviations. The fourth hypothesis supposes that inter-ply effects have a limited effect on the in-plane centroid path. The last assumption refers to the out-of-plane centroid, tow area and tow aspect ratio that are quantified from a unit cell sample. Although invalidation of this assumption would be surprising, additional quantification over longer-range samples would be reassuring.

For the subject 2/2 twill textile composite, the generation of short-range deviations $\{z, A, AR, \theta\}$ are exemplified by the Markov Chain algorithm since for each of these tow path parameters no cross-correlation is observed while the data on correlation are not very rich and does not necessarily need a more elaborated method. The long-range deviations of $\{\rho\}$ are produced using the cross-correlated Series Expansion method since significant cross-correlation between sets of tows are found with much more information collected about the correlation structure.

*5.4.2. Average trends*

An average reinforcement description of the textile is acquired by (i) interpolation of the individual average periodic and handling trends of each tow path parameter to the equidistant grid locations over which the specimen is defined and (ii) combination of the different tendencies. Periodicity is exploited to construct the repetitive systematic trend of the short-range parameters along the entire lattice. Figure 11 displays the average reinforcement of the 2/2 twill woven composite.

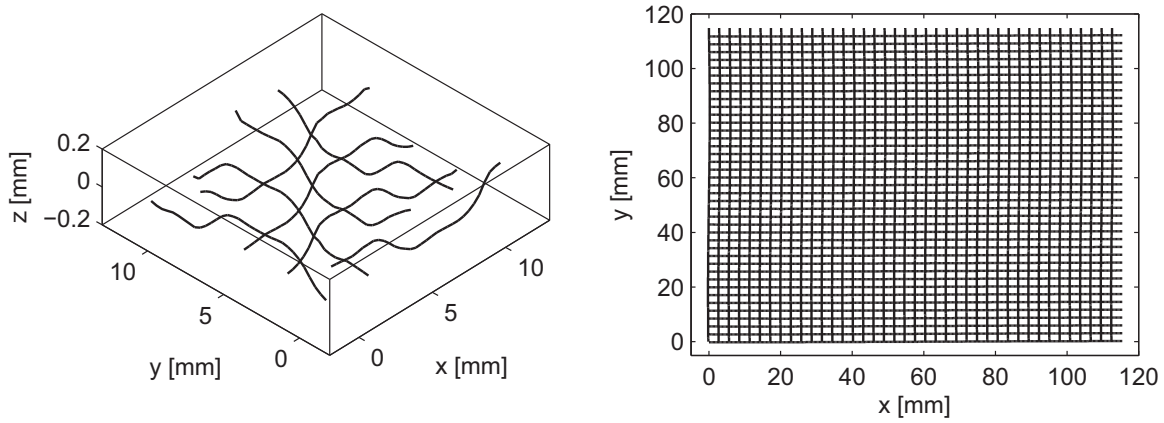


Figure 11: The average reinforcement description presented for the centroid coordinates at the short- and long-range, obtained by combining the average trends from figure 7 for all tow paths within the specimen.

*5.4.3. Simulation of auto-correlated deviations by the Monte Carlo Markov Chain method*

The Monte Carlo Markov Chain method has already been used to generate zero-mean tow centroid fluctuations of unit cells in [13], using the short-range data of tables 1 and 2 including the in-plane centroid position. The generalisation of the method for multiple unit cell structures is easily performed.

All short-range deviations of the subjected 2/2 twill woven composite $\{z, A, AR, \theta\}$ are produced using this approach. Any tow parameter of this set is generated over the grid of 320 points, as discussed in section 5.1. Based on the statistical information of these path parameters, it is sufficient to discretise the experimental deviations in twenty pieces ($m = 10$) with corresponding distribution vector. As a post-processing step, a smoothing operation is performed using information of $\pm 2$ neighbouring grid points. The procedure is able to reproduce the wavelengths of fluctuations as demonstrated in figure 12 for the warp out-of-plane centroid coordinate.

A total of $4 \times 10^4$ warp and weft tows were created by the Markov Chain algorithm to construct $10^3$ long-range specimens. Reproduction of the experimental statistical data is demonstrated for the warp tows using the (i) combined data set, collecting the deviations of all $4 \times 10^4$ tows, and the (ii) data sets that represent tow data of single unit cells. No additional comparison of the single tow statistics is performed due to the lack of experimental

information of individual tows with a length spanning ten unit cells.

Figure 13 presents the auto-correlation graph of the experimental and simulated warp $z$-centroid for the combined data set. Calibration of $A_{trans}$ using only the nearest neighbours ($k = 1$) results in an exponential correlation course with minor fluctuations that crosses the zero-correlation boundary for large point spacings. This is in contrast with the experimental correlation information that is typified by data that fluctuate around a trend, a discrepancy that is mainly attributed to the limited size of the experimental data set. When the correlation

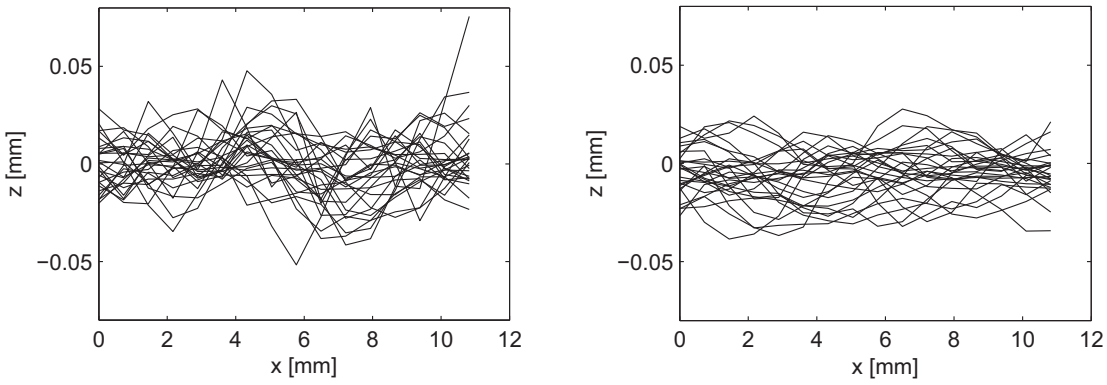


(a) Experiment (b) Simulation

Figure 12: Warp out-of-plane centroid deviations trend for 28 warp tows: (a) experimental vs. (b) smoothed deviations obtained from simulations.

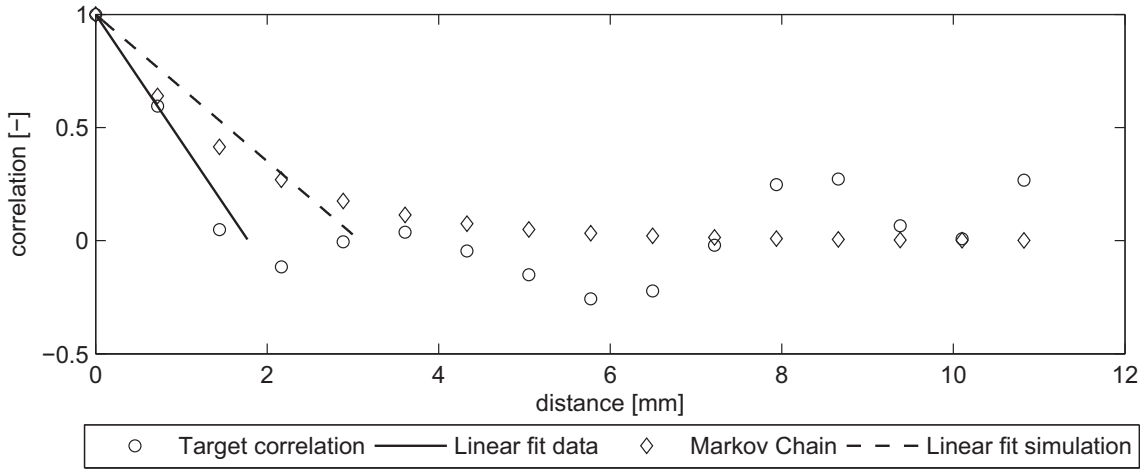


Figure 13: Correlation graph showing the experimental and simulated data of the warp $z$-centroid coordinate. A linear approximation of the first lag data is performed to deduce the correlation length.

length is approximated by a linear fit to the five nearest point spacings ($k \leq 5$), better agreement results in higher correlation lengths for the produced deviations, especially for tow parameters with a correlation length smaller than $5\nu$. The simulated standard deviation and correlation length for generated *z*-centroids and aspect ratio *AR* are shown by means of example in table 3. Standard deviations of all parameters are simulated with high accuracy ($\Delta < 0.12\%$), while the correlation length of the tow path parameters of the *z*-centroid show significant normalised errors from the target data ($\Delta = 73\%$). Some but not all of the normalised error $\Delta$ arises in the smoothing operation to remove short-wavelength noise: correlation lengths are slightly increased after the smoothing step, because neighbouring values are made more dependent.

Table 3: Standard deviation and auto-correlation length for the combined data set of warp *z* and *AR* deviations produced with the Markov Chain algorithm. Smoothed results are indicated by *sm*.

| | $\sigma_z$ [mm] | $\sigma_{AR}$ [-] | $\xi_z$ [mm] | $\xi_{AR}$ [mm] |
|---|---|---|---|---|
| Warp genus | 0.014 | 1.772 | 3.08 | 8.77 |
| $\Delta_{warp}$ | 0.11% | 0.12% | 73.16% | 20.90% |
| Warp genus - *sm* | 0.013 | 1.755 | 3.65 | 10.86 |
| $\Delta_{warp-sm}$ | 5.84% | 1.09% | 104.79% | 49.61% |

In addition, the generated and experimental average unit cell standard deviation and auto-correlation length are compared. Unit cell statistics are computed by identification of tows belonging to a single unit cell in the virtual specimen. The Markov Chain permits a good comparison in average values for all short-range parameters as presented in table 4. The generated unit cell standard deviations and auto-correlation lengths are centred around the target values, for both warp and weft tows. This is demonstrated for the warp *z*-centroid coordinate in figure 14. Similar to the results in [13], smoothing has limited effect on the unit cell standard deviation, while a high variance is observed for the non-smoothed and smoothed correlation lengths. The sensitive calculation of the correlation length as linear approximation of the first lags in the auto-correlation graph and the relatively small number

of data points (128 per unit cell) are likely sources of the discrepancy between generated and experimental correlation lengths. As indicated in table 4, the normalised difference $\Delta$ increases substantially for the smoothed statistics to around 10% for the standard deviation and from 50% till 73% for the correlation lengths of $z$ and $AR$.

The modest errors in generated standard deviations and the larger errors in generated correlation lengths can be reduced to acceptably small levels by a simple expedient [40]:

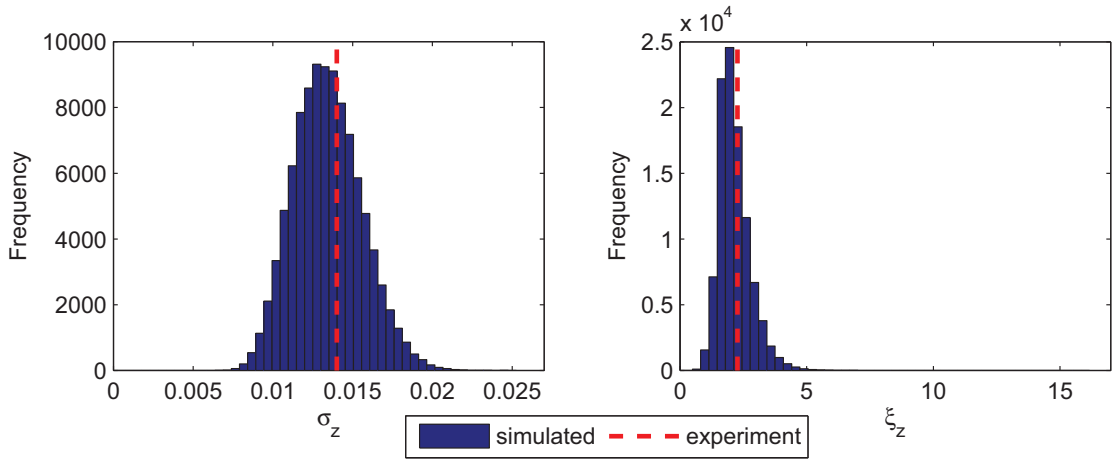


(a) Statistics of non-smoothed deviations

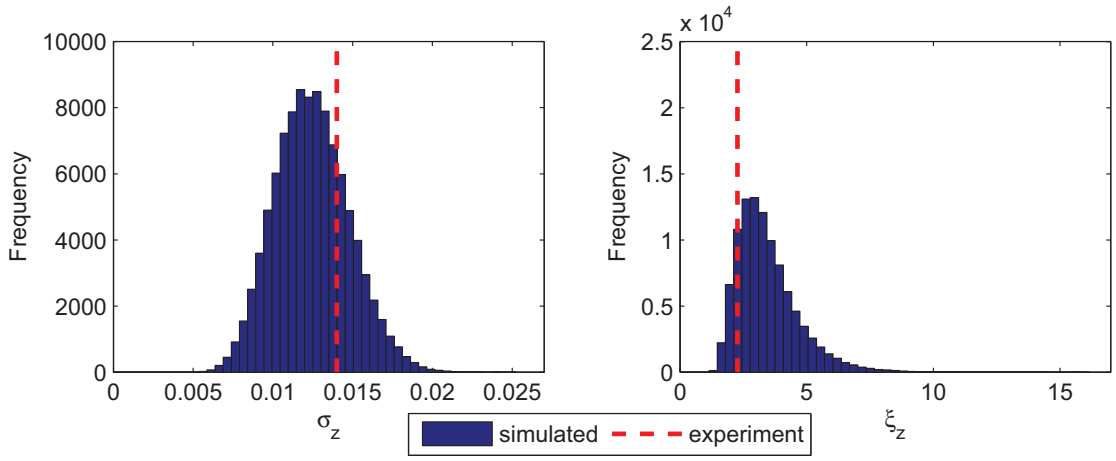


(b) Statistics of smoothed deviations

Figure 14: The unit cell statistics of the generated out-of-plane warp centroid positions (a) without and (b) with smoothing. Simulated data achieve the target statistics on average. When smoothing is applied, the simulated standard deviations are slightly affected, while all correlation lengths are increased.

if the target values used to calibrate the Markov Chain generator are shifted by a suitable amount, the generated statistics can be made to match the actual desired target statistics very well. The required shift can usually be found in a single iteration, because each generated variance or correlation length is approximately proportional to the value used for calibration of the Markov Chain.

Table 4: Mean of the standard deviation and auto-correlation length of the warp *z* and *AR* deviations belonging to single unit cells, produced with the Markov Chain algorithm. Smoothed results are indicated by *sm*.

| | $<\sigma_z>$ [mm] | $<\sigma_{AR}>$ [-] | $<\xi_z>$ [mm] | $<\xi_{AR}>$ [mm] |
|---|---|---|---|---|
| Target [17] | 0.014 | 1.774 | 2.27 | 6.84 |
| Warp tows | 0.013 | 1.569 | 2.15 | 7.00 |
| $\Delta_{warp}$ | 4.29% | 11.56% | 5.29% | 2.32% |
| Warp tows - *sm* | 0.013 | 1.540 | 3.45 | 11.82 |
| $\Delta_{warp-sm}$ | 10.71% | 13.22% | 51.78% | 72.82% |

### *5.4.4. Simulation of auto- and cross-correlated deviations by the cross-correlated Karhunen-Loève Series Expansion*

This technique is employed to simulate the in-plane centroid position $\{\rho\}$, which is the only tow path parameter in the considered 2/2 twill woven composite that is cross-correlated with adjacent tows. It is also the only parameter which possess a long-range trend. The Series Expansion is performed separately for warp and weft genus with forty individual tows per genus in one specimen ($N_j = 40$), equidistantly spaced over ten times the periodic length in *y*-direction for the warp genus or in *x*-direction for the weft genus. Each set of long-range tow path deviations $\tilde{H}_j(x)$ is described over a sparse equidistant grid of forty-one points ($N_i = 41$) that span at least ten times the periodic length of its tow direction.

The auto-correlation and cross-correlation matrices are constructed from the fitted correlation functions to the computed Pearson's correlation values for different point spacings, deduced in section 4.2 and summarised in table 5. Auto-correlation is obtained by projecting the auto-correlation functions onto the grid of forty-one points representing the tow

length, while the cross-correlation functions are projected onto the grid of forty points representing the in-plane positions of each individual tow path. In this procedure, it is assumed that the auto-correlation data only depend on the separation of points in the tow direction, while cross-correlation data depend only on the separation of points in the direction normal to the tows. In a last step, the generated long-range deviations, defined on a sparse grid of forty-one points, are interpolated at all locations on the finer grid of 320 points.

Table 5: Input correlation functions and applied truncation for simulating the in-plane fluctuations.

| | Warp tows | Weft tows |
|---|---|---|
| Auto-correlation $C_{auto}$ | $\sigma^2_{wa} \exp\left(-\frac{\tau_x}{\xi^{warp}_{auto}}\right)$ | $\sigma^2_{we} \exp\left(-\frac{\tau_x^2}{\xi^{weft^2}_{auto}}\right)$ |
| Cross-correlation $C_{cross}$ | $\exp\left(-\frac{\tau_x}{\xi^{warp}_{cross}}\right)$ | $\exp\left(-\frac{\tau_x^2}{\xi^{weft\ 2}_{cross}}\right)$ |
| $N_{var}$ | 33 | 4 |
| $N_{f,r}$ | 40 | 13 |

Realisations $\tilde{H}_j(x)$ of the in-plane centroids of warp and weft tows are computed using the truncated series of equation 14. After sorting the eigenvalues, only the $N_{var}$ or $N_{f,r}$ largest eigenvalues and corresponding eigenvectors are considered in the procedure instead of respectively $N_i$ and $N_j$. An appropriate measure of the captured variability is given by

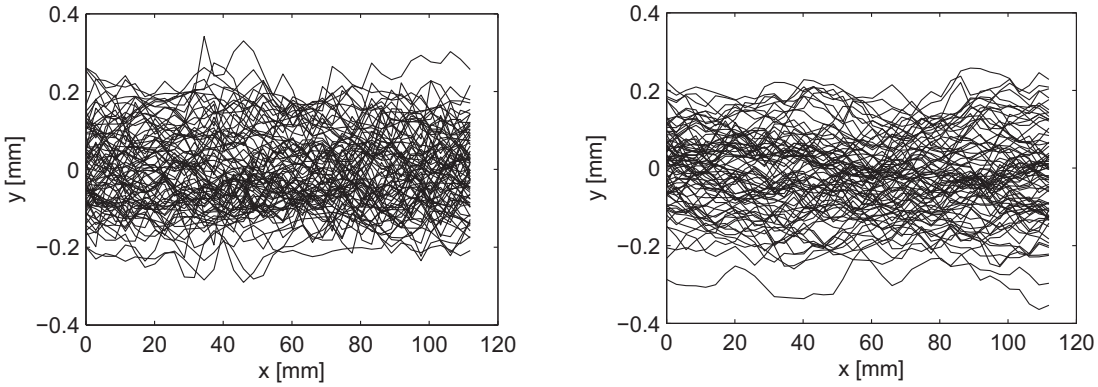


(a) Experiment (b) Simulation

Figure 15: Warp in-plane centroid deviations trend for 80 warp tows: (a) experimental vs. (b) simulated deviations.

the normalised sum (or truncation error) $\varrho$ which is fixed to minimum 0.9975:

$$\varrho = \frac{\sum_{i=1}^{N_{red}} \lambda_i}{\sum_{i=1}^{N} \lambda_i} \geq 0.9975 \tag{17}$$

with $N_{red}$ equal to $N_{var}$ or $N_{f,r}$. The applied truncation for warp and weft deviations is related to wavelength of the variations in each direction and is given in table 5. Throughout the procedure, no correlation control techniques are considered to reduce possible spurious correlation between the random variables $\chi_{j,i}^{D}$. A sensitivity analysis concluded that this additional operation does not add in significant accuracy for the resulting statistics. Additional side points to the considered grid of the random field are not foreseen since no disturbance in the produced deviation values are observed at the beginning and end of the field.

In-plane centroid fluctuations are generated for $4 \times 10^4$ tows of each genus. The short wavelength of the experimental warp deviations and long wavelength of the measured weft variations are reproduced by the simulations. The correspondence for the warp in-plane deviation trend is demonstrated in figure 15. In contrast to the deviations produced with the Markov Chain algorithm in section 5.4.3, no additional smoothing operation is needed. Quantification of the spikes in the produced fluctuations concludes a less spiked path than observed in the experiments. This is not only attributed to the Series Expansion technique, but also to the normality assumption of the in-plane deviations which diminishes the presence of larger spikes in the simulated path.

The conformity between the experimental and simulated statistics is validated for the warp tows using data of thousand generated virtual specimens. This information is investigated for the (i) combined data set, (ii) individual specimens consisting of hundred unit cells and (iii) individual 1-D fields, each representing one tow with a length of ten unit cells.

Statistics of the combined data set are precisely reproduced with normalised differences $\Delta$ for standard deviation $\sigma$ and correlation lengths $\xi_{auto}$, $\xi_{cross}$ which are less than 1% (table 6). Target correlation functions (table 5) and simulated correlation functions perfectly overlap with small differences for the largest lag spacings, shown in figure 16 for the warp

auto- and cross-correlation graph.

When the statistical data per specimen ($< \sigma >$, $< \xi_{auto} >$, $< \xi_{cross} >$) are considered, again good correspondence is obtained as indicated in table 6. The produced auto- and cross-correlation lengths for the warp tows of all thousand reinforcement descriptions are shown in figure 17. All generated correlation lengths have normalised errors $\Delta$ which are less than 3.48% for the standard deviation and maximum 1.72% for the correlation lengths.

Table 6: Standard deviation and correlation lengths for the (i) combined data set of in-plane positions and (ii) mean of the individual specimens, generated with the cross-correlated Series Expansion technique.

| | $\sigma^{comb}$ [mm] | $< \sigma^{spec} >$ [mm] | $\xi^{comb}_{auto}$ [mm] | $< \xi^{spec}_{auto} >$ [mm] | $\xi^{comb}_{cross}$ [mm] | $< \xi^{spec}_{cross} >$ [mm] |
|---|---|---|---|---|---|---|
| Warp tows | 0.106 | 0.103 | 115.81 | 114.00 | 4.54 | 4.42 |
| $\Delta_{warp}$ | 0.09% | 3.48% | 0.80% | 0.78% | 1.03% | 1.72% |

An overview of the individual warp field statistics, in terms of standard deviation and auto-correlation length, is presented in table 7. The experimental information of the individual tow standard deviation and correlation information is computed from arranging the data in [14]. While the generated standard deviation is obtained within 3% error, the produced auto-correlation length only approximates the target value with similar order of magnitude.

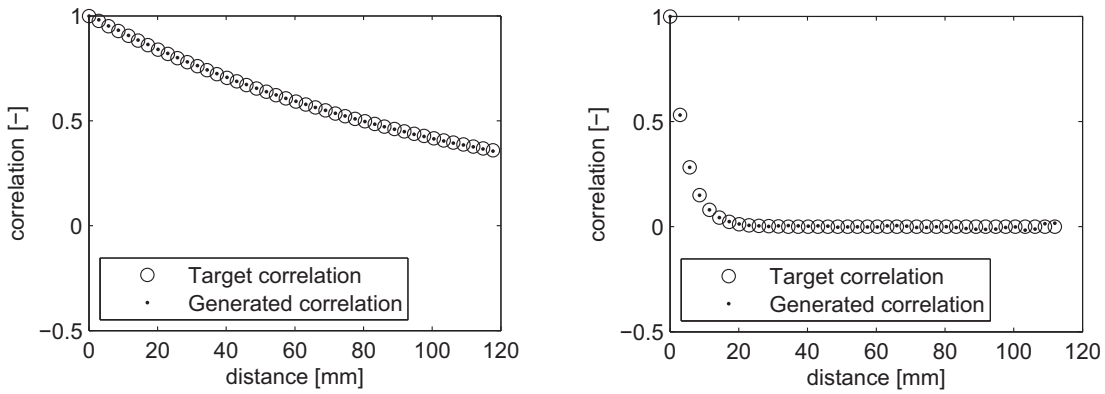


(a) Auto-correlation (b) Cross-correlation

Figure 16: Comparison of the warp input and simulated (a) auto-correlation and (b) cross-correlation functions. A perfect fit is obtained with minor fluctuations for the highest point spacings.

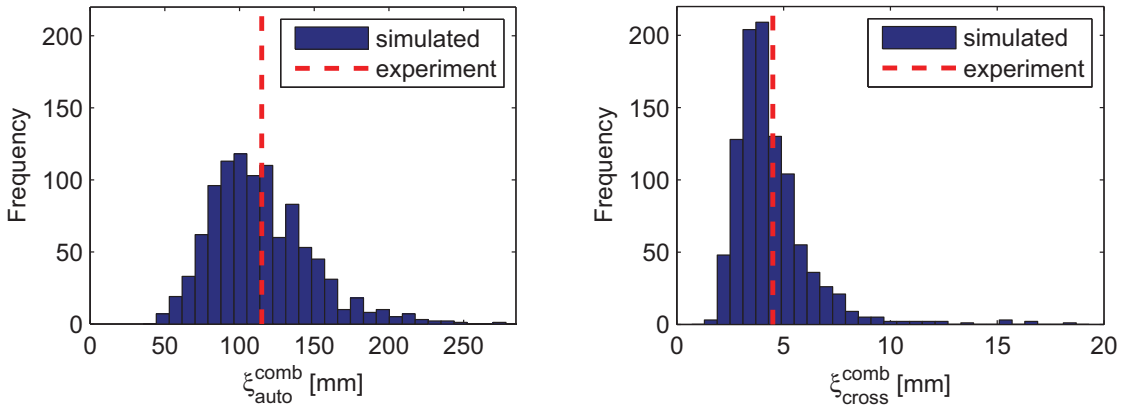


(a) Auto-correlation (b) Cross-correlation

Figure 17: Simulated (a) auto- and (b) cross-correlation lengths of the warp in-plane centroids. The experimental value is simulated on average.

Latin Hypercube sampling of the independent deviations $\eta_r$ ensures a good similarity with the target mean and standard deviation. The difference in target and simulated correlation length is due to the normality assumption of the deviations distribution and the ideal fitted input correlation functions. These provoke the duplication of the statistical information on the individual tow level.

Table 7: Standard deviation and correlation lengths for individual 1-D random fields, representing the in-plane centroid, produced with the cross-correlated Series Expansion technique.

| | $\sigma^{target}$ [mm] | $\sigma^{1D}$ [mm] | $\xi^{target}_{auto}$ [mm] | $\xi^{1D}_{auto}$ [mm] |
|---|---|---|---|---|
| Warp tows - *mean* | 0.051 | 0.053 | 20.69 | 32.06 |
| $\Delta_{warp,mean}$ | - | 2.93% | - | 54.93% |

## 6. Construction of virtual specimens in a geometrical modelling software (step 3)

The last step of the multi-scale framework (figure 2) creates virtual specimens with random geometry that possesses both long-range and short-range deviations with the appropriate auto- and cross-correlations. In this paper, we exemplify this step by using the commercially available WiseTex software [16]. The tow path description of a nominal WiseTex

model is overwritten by the stochastic tow path realisations, which are built as combination of the average trend with the generated zero-mean deviations for each tow path parameter. The WiseTex XML-structure is used to overwrite the tow path information since it permits scripting of local reinforcement information without the need of understanding the internal computational procedure [58]. In addition to the tow path description, other path information of the nominal model is updated such as the path length and the orientation vectors that fix each cross-section along the path in space [13, 59, 4].

Figure 18 compares a nominal model with a generated stochastic specimen of the 2/2 twill woven composite. A substantially different reinforcement description is observed. In contrast to the nominal model where warp and weft tows are following straight paths, the random model shows a significant difference in the in-plane centroid mobility for the warp and weft tows: weft tows are more variable and possess clustering behaviour between neighbouring tows. This results in spatial distribution of the open space between two neighbouring tows which varies locally. The detailed image of an arbitrary unit cell shows the variation in the out-of-plane centroid position and tow cross-sectional variations.

## 7. Discussion

Generally, the statistics of a stochastic textile can be more completely replicated using methods that use all available auto-correlation information and incorporate cross-correlations as well, such as the Series Expansion technique and the modified Fourier transform detailed above. These methods calibrate the generation procedure by matching the variation of correlations between pairs of points whose separation rises from effectively zero to the span of the data. In contrast, the Markov Chain method targets only the initial, approximately linear decrease in the correlation between data from pairs of points as the separation of the pair increases from zero. It is used when data are not sufficiently rich to support the more detailed analysis of the Series Expansion or modified Fourier methods, and combined with the simple iteration described in section 5.4.3 to reduce errors due to the discreteness of the representation or smoothing operations, the Markov Chain method is reasonably accurate

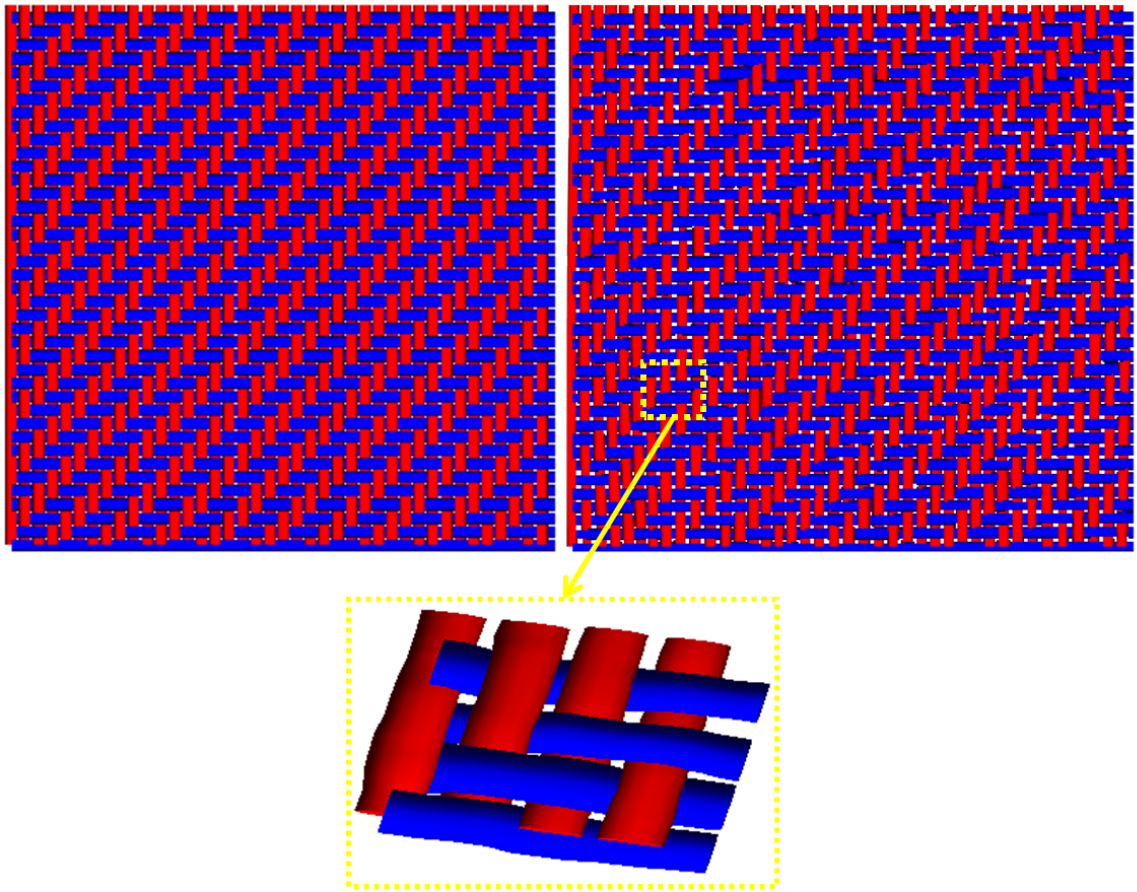

Figure 18: WiseTex representation of a nominal and stochastic virtual specimen. Warp and weft tows are respectively oriented horizontally and vertically.

and expedient. For data analyzed to date, the simple concept of the transition matrix that underlies the Markov chain procedure has proven very appropriate for the spatially limited data available from micro-CT experiments [49, 40, 17, 13], where correlation information is only reliably defined for pairs of data points with small separations. In contrast, the data acquired using optical imaging or digital image correlation cover much larger spatial ranges [14, 15], supporting the detail required by the Series Expansion or modified Fourier methods.

The proposed methodology is devoted to typify the spatial geometrical randomness at the meso- and macro-scale of high-performance composites, mainly used in aerospace applications. Fluctuations at the micro-level, such as fibre distribution and resin content inside

a single tow, remain to be included. Fibre-scale variations have been identified using micro-CT imaging [44, 45, 46] and may well be related to those at higher scales, since the spatial structure of stochastic fibre bundles may be implicated in the constitutive behavior of the bundles [46], which will influence the bundle (or tow) shape when woven into preforms.

In future work, the virtual specimens demonstrated here can be employed to predict the effect of geometrical variability on the macroscopic mechanical properties. The precise description of geometrical variability over the composite allows one to (i) predict its mechanical performance, such as stiffness, to define a quantitative measure of the spatial variation over the structure, (ii) perform damage simulations with a higher fidelity, or (iii) precisely simulate the resin impregnation of component-size fabrics. The random specimens in the WiseTex format, without any adjustments, are directly compatible with tools for micromechanical analysis such as stiffness evaluation [22, 4] and permeability simulations [60]. Other simulations, especially damage investigation, require the FE representation of the random specimens. However, when transforming the WiseTex model into a FE model, small adaptations are required of the tow path description since limited interpenetration appears in the virtual specimens. Within these models, tows need to be translated until the interpenetration is removed, but such that topological rules stay satisfied [59, 41] and statistical information is not altered.

## 8. Conclusions

A generic multi-scale framework is developed to generate realistic virtual textile specimens. The aim of this approach is to deliver large textile models, i.e. consisting of multiple unit cells, with a reinforcement structure that possesses the same statistical information as quantified from the experimental samples. First, an experimental methodology is presented to characterise the geometrical variability in terms of the centroid coordinates and cross-sectional parameters on the short-range (meso-scale) and long-range (macro-scale). Non-destructive state-of-the-art inspection techniques such as X-ray micro-computed tomography, optical imaging or digital image correlation are applied to measure the fabric

architecture in a reliable and efficient way across the composite volume. The inherent scatter of each tow path parameter in each tow direction is quantified in terms of an average trend, standard deviation and correlation information by applying the reference period collation method. Secondly, a stochastic multi-scale modelling approach is developed to reproduce the measured variation in the tow reinforcement within the unit cell and between neighbouring unit cells. Random instances of tow paths are acquired by combining the deduced average trends with generated zero-mean fluctuations possessing the experimental standard deviation and correlation lengths on average. Zero-mean auto-correlated deviations are produced by the Monte Carlo Markov Chain for textile structures or a Series Expansion technique, while uncertain quantities that are dependent along and between tow paths (auto- & cross-correlated) are generated using a cross-correlated Series Expansion method or a Fourier Transform method in combination with a Markov Chain algorithm. In the last step, virtual composite specimens with random fibre architecture are created in geometrical modelling software, such as the commercially available WiseTex software, using an intrusive approach. Nominal tow path descriptions are overwritten with realistic tow representations obtained from the previous step, while preserving the original fibre mechanics and matrix properties. Concepts and procedures of this framework are developed for woven composites, but only minor modifications are required for other textile topologies than woven structures.

The entire roadmap is demonstrated on a carbon-epoxy 2/2 twill woven composite produced by RTM. Virtual specimens are simulated that span a region of ten by ten unit cells and are representative for a ply within a laminate. The preceded experimental characterisation concludes that the geometrical variability of this high-performance textile is significant with substantial differences for warp and weft direction attributed to the manufacturing process of the weave. The in-plane coordinate is subjected to the largest variation exceeding the unit cell dimensions and is the only property of the tow path which is cross-correlated with neighbouring tows of the same type. Based on this information, deviations of the out-of-plane centroid $z$, aspect ratio $AR$ and area $A$ are produced using the Monte Carlo

Markov Chain method, while the cross-correlated in-plane position $\rho$ is generated by the cross-correlated Series Expansion procedure. A good comparison in terms of wavelengths and extreme values is obtained between the experimental and simulated deviations trends for all properties. Further, all simulated tow deviations achieve the target statistics on average. The acquired virtual models in the WiseTex software can be further exploited for studies on the reliability and quality of composites.

**Acknowledgements**

This study is supported by the Flemish Government through the Agency for Innovation by Science and Technology in Flanders (IWT) and FWO-Vlaanderen.

**References**

[1] Cox B, Yang Q. In quest of virtual tests for structural composites. Science 2006;314(5802):1102–7.

[2] Graham-Brady L, Arwade S, Corr D, Gutierrez M, Breysse D, Grigoriu M, et al. Probability and materials: from nano- to macro-scale: a summary. Probabilistic Engineering Mechanics 2006;21(3):193–9.

[3] Charmpis DC, Schuëller GI, Pellisetti MF. The need for linking micromechanics of materials with stochastic finite elements: A challenge for materials science. Computational Materials Science 2007;41(1):27–37.

[4] Lomov S, Huysmans G, Luo Y, Parnas R, Prodromou A, Verpoest I, et al. Textile composites: modelling strategies. Composites Part A 2001;32(10):1379–94.

[5] Mehrez L, Doostan A, Moens D, Vandepitte D. Stochastic identification of composite material properties from limited experimental databases, part 1: Experimental database construction. Mechanical Systems and Signal Processing 2012;27:471–83.

[6] Chamis C. Probabilistic simulation of multi-scale composite behaviour. Theoretical and applied facture mechanics 2004;41(1-3):51–61.

[7] Sriramula S, Chryssanthopoulos MK. Quantification of uncertainty modelling in stochastic analysis of FRP composites. Composites Part A 2009;40(11):1673–84.

[8] Kamiński M. Computational mechanics of composite materials: sensitivity, randomness and multiscale behaviour. London: Springer; 2005.

[9] Ostoja-Starzewski M. Microstructural randomness and scaling in mechanics of materials. London: Chapman & Hall; 2008.

[10] Schuëller G. A state-of-the-art report on computational stochastic mechanics. Probabilistic Engineering Mechanics 1997;12(4):197–321.

[11] Ghanem R, Spanos P. Stochastic Finite Elements: a Spectral Approach. New York: Springer-Verlag; 2000.

[12] Dadkhah M, Flintoff J, Kniveton T, Cox B. Simple models for triaxially braided composites. Composites 1995;26(8):561–77.

[13] Vanaerschot A, Cox B, Lomov S, Vandepitte D. Stochastic multi-scale modelling of textile composites based on internal geometry variability. Computers & Structures 2013;122:55–64.

[14] Vanaerschot A, Cox B, Lomov S, Vandepitte D. Simulation of the cross-correlated positions of in-plane tow centroids in textile composites based on experimental data. Composite structures 2014;116:75–83.

[15] Rossol M, Fast T, Marshall D, Cox B, Zok F. Characterizing in-plane geometrical variability in textile ceramic composites. Journal of the American Ceramic Society 2015;98(1):205–13.

[16] Verpoest I, Lomov SV. Virtual textile composites software wisetex: Integration with micro-mechanical, permeability and structural analysis. Composites Science and Technology 2005;65(15-16):2563–74.

[17] Vanaerschot A, Cox B, Lomov S, Vandepitte D. Stochastic framework for quantifying the geometrical variability of laminated textile composites using micro-computed tomography. Composites Part A 2013;44:122–31.

[18] Vanaerschot A, Cox B, Lomov S, Vandepitte D. Stochastic characterisation of the in-plane tow centroid in textile composites to quantify the multi-scale variation in geometry. In: Proceedings of the IUTAM Symposium on Multiscale Modeling and Uncertainty Quantification of Materials and Structures. Santorini, Greece: Springer; 2014, p. 187–202.

[19] Maître OL, Knio O. Spectral methods for uncertainty quantification with applications to computational fluid dynamics. Springer; 2010.

[20] Metropolis N, Ulam S. The monte carlo method. Journal of the American Statistical Association 1949;24:335–41.

[21] Desplentere F, Lomov SV, Woerdeman DL, Verpoest I, Wevers M, Bogdanovich A. Micro-CT characterization of variability in 3D textile architecture. Composites Science and Technology 2005;65(13):1920–30.

[22] Olave M, Vanaerschot A, Lomov S, Vandepitte D. Internal geometry variability of two woven composites and related variability of the stiffness. Journal of Polymer Composites 2012;33(8):1335–50.

[23] Cox B, Dadkhah M. The macroscopic elasticity of 3D woven composites. Journal of Composite Materials 1995;29(6):785–819.

[24] Argon A. Treatise on Materials Science and Technoloy. NY and London: Academic Press; 1972.

[25] Cox B, Dadkhah M, Morris W, Flintoff J. Failure mechanisms of 3D woven composites in tension, compression and bending. Acta Metallurgica et Materialia 1994;42(12):3967–84.

[26] Slaugther W, Fleck N. Compressive faftigue of fibre composites. Journal of the Mechanics and Physics of Solids 1993;41(8):1265–84.

[27] Dadkhah M, Morris W, Cox B. Compression-compression fatigue in 3D woven composites. Acta Metallurgica et Materialia 1995;43(12):4235–45.

[28] Fleck N, Shu J. Microbuckle iniation in fibre composites: a finite element study. Journal of the Mechanics and Physics of Solids 1995;43(12):1887–918.

[29] Kregers A, Melbardis Y. Determination of the deformability of three-dimensionally reinforced composites by the stiffness averaging method. Mechanics of Composite Materials 1978;14(1):1–5.

[30] Tarnopolskii Y, Polyakov V, Zhigun I. Composite materials reinforced with a system of three straight mutually orthogonal fibres. Polymer Mechanics 1973;9(5):753–9.

[31] Xu J, Cox B, McGlockton M, Carter W. Binary Model of textile composites: II elastic regime. Acta Metallurgica et Materialia 1995;43(9):3511–21.

[32] Sejnoha M, Zeman J. Micromechanical modeling of imperfect textile composites. International Journal of Engineering Science 2008;46(6):513–26.

[33] Zeng X, Brown L, Endruweit A, Matveev M, Long A. Geometrical modelling of 3d woven reinforcements for polymer composites: prediction of fabric permeability and composite mechanical properties. Composites Part A 2014;56:150–60.

[34] Endruweit A, Long AC. Influence of stochastic variations in fibre spacing on the permeability of bi-directional textile fabrics. Composites Part A 2006;37(5):679–94.

[35] Abdiwi F, Harrison P, Koyama I, Yu W, Long A, Corriea N, et al. Characterising and modelling variability of tow orientation in engineering fabrics and textile composites. Composites Sciences and Technology 2012;72(9):1034–41.

[36] Skordos AA, Sutcliffe MPF. Stochastic simulation of woven composites forming. Composites Science and Technology 2008;68(1):283–96.

[37] Yushanov S, Bogdanovich A. Fiber waviness in textile composites and its stochastic modeling. Mechanics of Composite materials 2000;36(4):297–318.

[38] Vořechovský M. Simulation of simply cross correlated random fields by series expansion methods. Structural Safety 2008;30(4):337–63.

[39] Phoon K, Huang H, Quek S. Comparison between karhunen-loeve and wavelet expansions for simulation of gaussian processes. Computers & structures 2004;82(13-14):985–91.

[40] Blacklock M, Bale H, Begley M, Cox B. Generating virtual textile composite specimens using statistical data from micro-computed tomography: 1D tow representations for the Binary Model. Journal of the Mechanics and Physics of Solids 2012;60(3):451–70.

[41] Rinaldi R, Blacklock M, Bale H, Begley M, Cox B. Generating virtual textile composite specimens using statistical data from micro-computed tomography: 3D tow representations. Journal of the Mechanics and Physics of Solids 2012;60(8):1561–81.

[42] Cox B, Bale H, Begley M, Blacklock M, Do B, Fast T, et al. Stochastic virtual tests for high-temperature ceramic matrix composites. Annual Review of Materials Research 2014;44:1–51.

[43] McGlockton M, Cox B, McMeeking R. A binary model of textile composites: III High failure strain and work of fracture in 3D weaves. Journal of the Mechanics and Physics of Solids 2003;51(8):1573–600.

[44] Przybyla C, Simmons J, Zawada L, Godar T, Bricker S, Jackson M, et al. Statistical characterization of SIC/SIC ceramic matrix composites at the filament scale with bayesian segmentation, hough transform feature extraction, and pair correlation statistics. In: SAMPE 2013 Proceedings: Education & Green Sky - Materials Technology for a Better World. Long Beach, CA: SAMPE; 2013,.

[45] Czabaj M, Riccio M, Whitacre W. Numerical reconstruction of graphite/epoxy composite microstructure based on sub-micron resolution X-ray computed tomography. Composites Science and Technology 2014;105:174–82.

[46] Fast T, Scott A, Bale H, Cox B. Topological and euclidean metrics reveal spatially nonuniform structure in the entanglement of stochastic fiber bundles. Journal of Materials Science 2015;50(6):2370–98.

[47] Ko F. Preform fiber architecture for ceramic-matrix composites. Ceramic Bulletin 1989;68(2):401–14.

[48] Marshall D, Cox B. Integral textile ceramic structures. Annual Review of Materials Research 2008;38:425–43.

[49] Bale H, Blacklock M, Begley M, Marshall D, Cox B, Ritchie R. Characterizing three-dimensional textile ceramic composites using synchrotron x-ray micro-computed-tomography. Journal of the American Ceramic Society 2012;95(1):392–402.

[50] Vanaerschot A, Panerai F, Cassell A, Lomov S, Vandepitte D, Mansour N. Uncertainty quantification of a 3-d woven carbon fabric for the adept thermal protection system. Submitted to Composites Science and Technology 2016;.

[51] Hexcel . HexForce G0986 SB 1200 - Product Data Hexcel. 2014.

[52] Blacklock M, Shaw J, Zok F, Cox B. Deformation mechanisms of dry textile preforms under mixed compressive and shear loading. Submitted to Composites 2015;.

[53] Sudret B, Kiureghian AD. Stochastic finite element methods and reliability: a state-of-the-art report. Department of civil & environmental engineering, University of California Berkeley; 2000.

[54] Jolliffe I. Principal Component Analysis. Berlin: Springer-Verlag; 1986.

[55] Arnst M, Ghanem R, Soize C. Identification of bayesian posteriors for coefficients of chaos expansions. Journal of Computational Physics 2010;229(9):3134–54.

[56] Vořechovský M, Novák D. Correlation control in small-sample monte carlo type simulations 1: A simulated annealing approach. Probabilistic Engineering Mechanics 2009;24(3):452–62.

[57] Jiang Y, Chen X. Geometric and algebraic algorithms for modelling yarn in woven fabrics. Journal of the Textile Institute 2005;96(4):237–45.

[58] Lomov S, Verpoest I, Cichosz J, Hahn C, Ivanov D, Verleye B. Meso-level textile composites simulations: Open data exchange and scripting. Journal of Composite Materials 2014;48(5):621–37.

[59] Lomov S, Ivanov D, Verpoest I, Zako M, Kurashiki T, Nakai H, et al. Meso-FE modelling of textile composites: road map, data flow and algorithms. Composites Science and Technology 2007;67(9):1870–91.

[60] Verleye B, Croce R, Griebel M, Klitz M, Lomov S, Morren G, et al. Permeability of textile reinforcements: Simulation, influence of shear and validation. Composites Science and Technology 2008;68(13):2804–10.